Materials Advances

ROYAL SOCIETY OF CHEMISTRY

REVIEW

Check for updates

One bismuth three benefits: an overview of bismuth-based photocatalysts for energy conversion, environmental treatment and biomedical applications

Deng Long, [ID] Xinglin Yu, Wentao Li [ID]* and Sihan Ma [ID]*

A wide variety of bismuth-based photocatalysts are considered excellent candidates for energy conversion, environmental pollutant treatment and biomedical engineering applications and have attracted extensive attention owing to their unique electronic structural properties, good photoelectric response and safety. However, the pristine bismuth-based nanomaterials still have some limitations in the comprehensive application, *e.g.* their fast charge recombination restricts photoelectric utilization efficiency, whereas their low quantum yield and low light absorption capacity restrict catalytic activity. Therefore, reliable functional modification of bismuth-based materials is performed to achieve a wider range of applications in many reports. In this review, the research progress on bismuth-based photocatalysts in energy, environment and biomedicine is summarized in detail. Furthermore, in order to effectively promote the overall understanding and application of bismuth-based materials, the functional modification methods are also reviewed in this review. Finally, we evaluated the opportunities and challenges encountered by bismuth-based photocatalysts, aiming to provide guidance for the rapid development of bismuth-based photocatalysts.

1. Introduction

The rapid development of science and technology has brought about the problems of environmental pollution, energy crisis and medical shortage, and it is urgent to develop new technologies to solve these problems in order to achieve the long-term sustainable development of society.[1] In the

development of science and technology, nanomaterials have shown great potential in energy, environment and medical treatment due to their unique physical and chemical properties such as large specific surface area, small size effect, quantum effect and quantum confinement. Nanomaterials have been widely researched and applied because of their unique physical and chemical properties, including their large specific surface area, small size effect, quantum effect and quantum confinement. Among the most popularly used nanomaterials, semiconductor

College of Big Data and Information Engineering, Guizhou University, Guiyang 550025, China. E-mail: wtli@gzu.edu.cn, mash16@lzu.edu.cn

Deng Long received his PhD in Energy and Chemical Industry from Xiamen University in 2023. He is now working as a specially appointed professor at Guizhou University. During 2021 to 2022, he worked as a visiting scholar at the Chemistry Department of Humboldt-Universität zu Berlin. His current work includes the synthesis and modification of 2D materials for photocatalytic CO2 reduction and photodevices.

Deng Long

Xinglin Yu was born in Guizhou, China. He received his PhD from the School of Information Science and Technology, Southwest Jiaotong University, Sichuan, China, in 2022. He is currently Lecturer in the College of Big Data and Information Engineering, Guizhou University. His current research interests include gas/humidity sensors and novel electronic devices.
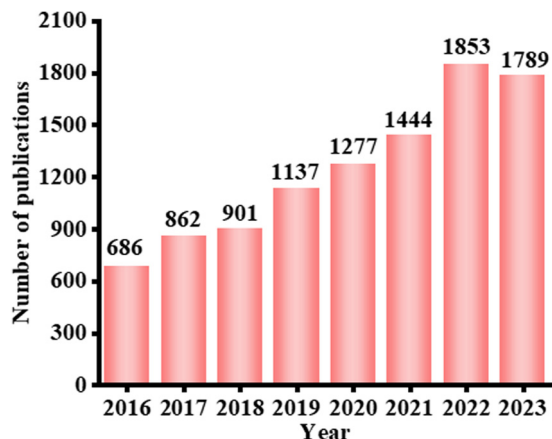
Xinglin Yu

Fig. 1 Number of published papers related to Bi-based photocatalysts from 2016 to 2023 (data collected on 8 March 2024, from a search performed on the Web of Science for "Bi cataly*" topics).

nanomaterials have received widespread application and attention owing to their relatively low price, abundant reserves and other advantages.[1,2] In particular, semiconductors can produce electrons and holes under photoexcitation and then interact with the surrounding media to produce reactive oxygen species to achieve photocatalytic degradation of environmental pollutants,[3–7] energy conversion involving water splitting,[8–10] HERs,[11–16] nitrogen fixation and removal,[17–19] CO_2 reduction,[20–27] photocatalytic ethylene synthesis,[28,29] and biomedical applications involving bactericidal activity[30–35] and treatment of diseases.[36–40] Thus, the emergence of semiconductor photocatalysts paves the way for overcoming environmental, energy and biomedical problems.

Bismuth-based photocatalysts, as potential light-triggered nano-semiconductors, can efficiently utilize light energy, and further, a broad spectrum of light absorption can be achieved from visible to near-infrared light, which have widely attracted attention in different fields.[41,42] Thus, it is not surprising that the number of published papers related to bismuth-based photocatalysts have grown at an incredible rate from 2016 to 2023 (Fig. 1). However, the photocatalytic activity of single structured bismuth-based photocatalysts is limited by carrier separation efficiency and light absorption capacity. Therefore, numerous reports have focused on structural modifications to enhance their optical properties and photocatalytic activity.

The crystal structure of bismuth-based materials can be divided into four types,[43] namely, the Sillen structure (BiOCl), Aurivillius structure (Bi_2WO_6), Sillen–Aurivillius structure, and bismuth chromate (Bi_2CrO_6), where the Sillen structure and Aurivillius structure are the two main types of bismuth-based catalysts, bismuth halide oxide (BiOX) and bismuth metal oxide (Bi_aAO_b). In the BiOX system, X represents mainly halogen elements such as Cl, Br and I, and the unique layered structure of this material is formed by the overlapping of $[Bi_2O_2]^{2+}$ layers and double halogen atomic layers. Under photoexcitation, the p orbital electrons of halogen elements will transfer to Bi 6p, and a strong internal electric field is formed between the bismuth oxygen layer and the halogen layer. Under the action of the internal electric field, the photogenerated charge carriers are efficiently separated, and more photogenerated electrons are gathered on the surface, thus promoting the photocatalytic activity or other applications like biomedical application, *etc.* On the other hand, in Bi_aAO_b, Bi-based semiconductors mainly include $BiVO_4$, Bi_2WO_6, Bi_2MoO_6, *etc.* and their derivatives such as $Bi_2O_2CO_3$ and $Bi_2O_2SO_4$, which have received continuous attention because of their excellent visible light absorption, suitable band gap and chemical stability. In addition, their specific crystal phase guarantees their electron transport capability over other photocatalysts.[44–47] Changes in morphological and structural properties resulted in different optical properties and catalytic activities. For instance, since the monolayer of Bi_2WO_6 contains W vacancies inside, a defect energy level is formed, making it responsive throughout the visible range.[48] Moreover, non-surface W defects can increase the donor density in the valence band and decrease the resistance of the material. Due to the special heterojunction structure of $[BiO]^+$–$[WO_4]^{2-}$–$[BiO]^+$, its electrons and holes are separated at the interface of WO_4 and BiO, and electrons will stop in the WO_4 layer, resulting in the enhancement of the reducing ability of electrons caused by the presence of W defects. In addition, bismuth-based materials with ultra-thin structures, only a single or a few microns thick, have sheet-like structures of large transverse

Wentao Li received her PhD from Northwest University in 2022. After a year of postdoctoral work at The Hong Kong Polytechnic University, she was appointed as a specially appointed professor at Guizhou University from 2023. Her current research focuses on the molecular design and synthesis of luminescent metal complexes and polymers for photofunctional applications.

Wentao Li

Sihan Ma is currently a specially appointed professor at Guizhou University. He received his PhD in Nuclear Engineering and Materials from Xiamen University in 2023. His research interests focus on the synthesis of bismuth-based nanomaterials and ion irradiation modification as well as their applications in photocatalytic degradation, antibacterial activity, and energy conversion.

Sihan Ma

dimensions, which can exhibit unique physicochemical and electronic properties owing to two-dimensional electron confinement.[49,50] Meanwhile, two-dimensional ultra-thin structures will show a large surface area and expose more surface-unsaturated coordination atoms, resulting in stronger and wider absorption of sunlight and target molecules.[51] Importantly, two-dimensional materials with atomic thickness can shorten the migration distance of photogenerated carriers and thus improve the efficiency of carrier transfer and separation.[42]

In the previous studies, researchers have adopted many strategies to improve the photocatalytic activity of bismuth-based photocatalysts and made important progress. At the same time, some reports have reviewed bismuth-based semiconductor photocatalysts, but they either focus on the preparation methods of bismuth-based materials, or simply summarize the modification methods, while the review of the mechanism and in-depth understanding of the improvement of photocatalytic performance is still relatively lacking. Importantly, there is little work to comprehensively summarize the extensive understanding of bismuth-based photocatalysts, including applications in the energy, environment and biomedical fields, which is not conducive to the rapid development and wide application of bismuth-based photocatalysts. In summary, the purpose of this work was not only to summarize the modification of

bismuth-based photocatalysts, but also to better understand the mechanism of photocatalytic performance improvement of these catalysts and the detailed reaction mechanism in practical applications. Finally, the development prospects and challenges of bismuth-based materials in the field of photocatalysis are discussed for boosting the development of bismuth-based photocatalysts.

2. Modification strategies for promoting photocatalytic activity

2.1 Impurity ion introduction

When impurity ions are introduced into the semiconductor, they will form a corresponding impurity level between the valence band (VB) and the conduction band (CB) of the semiconductor, which will affect the photogenerated carrier transition of the semiconductor.[52] Indirectly, due to the existence of impurity levels, the electron transition distance is shortened, and the corresponding bandgap is reduced, which is conducive to wide wavelengths of light absorption and improving the light absorption capacity. As shown in Fig. 2(a), the band structure of $Bi_2Ga_4O_9$ can be narrowed by introducing Fe^{3+} into its cavity.[53] Fe^{3+} can substitute the sites of Ga, in the tetrahedral structure,
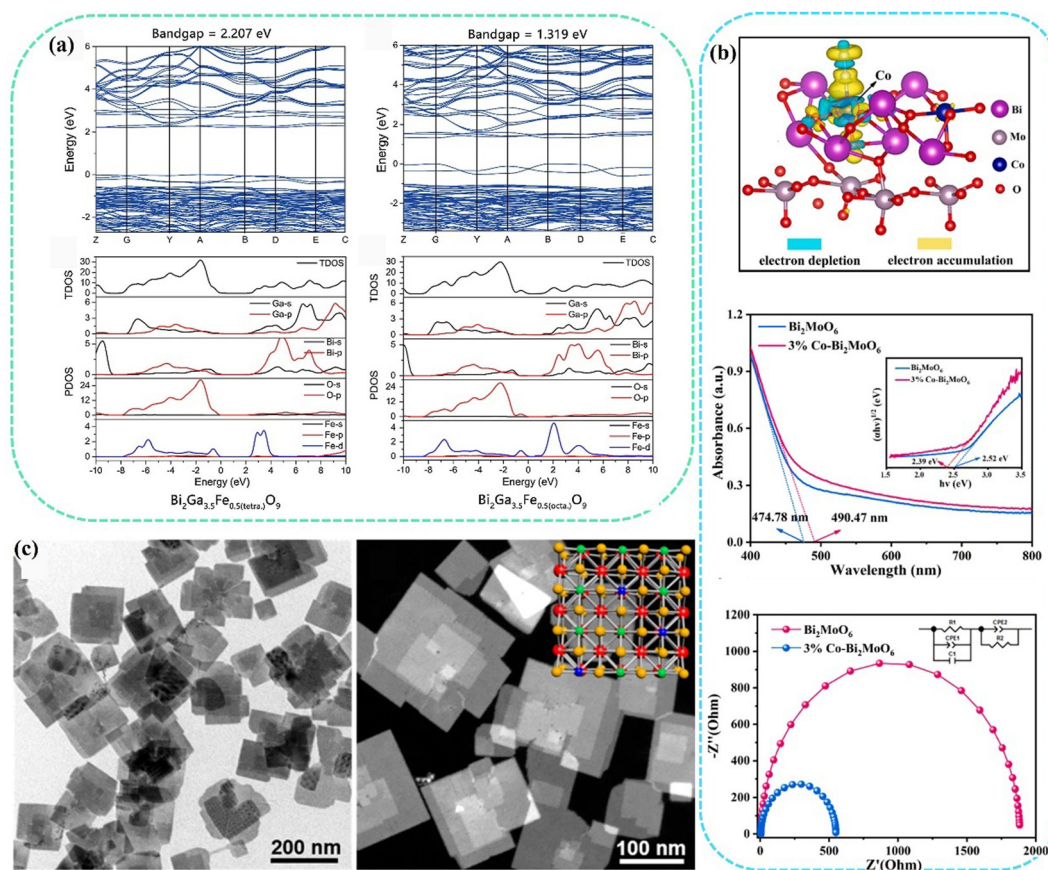

Fig. 2 (a) Calculated band structure and density of states for $Bi_2Ga_{3.5}Fe_{0.5}O_9$ with Fe^{3+}, either in the tetrahedral or octahedral cavity.[53] Copyright 2017, Elsevier. (b) Differential charge densities of $Co-Bi_2MoO_6$, UV-vis DRS spectra and EIS of Bi_2MoO_6 and 3% $Co-Bi_2MoO_6$.[55] Copyright 2023, Elsevier. (c) TEM images of BiOCl and BiOCl NSs-Fe-5%.[56] Copyright 2019, American Chemical Society.

_
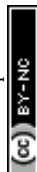
the band gap was narrowed from 2.935 eV to 2.207, and in the octahedral sites, the band gap can be even shortened to 1.319 eV, which can greatly increase the visible light application. Wang et al. reported Cu-doped Bi_2MoO_6 to carry out highly efficient photocatalytic nitrogen fixation.[54] Cu-doped Bi_2MoO_6 was synthesized by a simple solvothermal method. The effect of Cu doping on the performance of Bi_2MoO_6 was studied in detail. The results showed that the valence state of Cu is +2, replacing the position of Bi^{3+}. Cu doping has negligible effect on the morphology of Bi_2MoO_6, but a significant effect on the band structure. The bandgap is slightly narrowed and the conduction band is raised, leading to the production of more electrons and stronger reducibility caused by Cu doping of Bi_2MoO_6. Importantly, Cu doping reduced the work function and improved the charge separation efficiency, which was thought to be the key reason for enhancing photoactivity. In addition, the Cu-Bi_2MoO_6 catalyst had high adsorption and activation capacity for N_2. Under the combined effect of the above changes, Cu-Bi_2MoO_6 showed higher photocatalytic efficiency than Bi_2MoO_6. Doping with different types of ions can adjust the active sites to improve photocatalysis. Yang et al. innovatively employed Co as a dopant to construct the Co-doped Bi_2MoO_6.[55] Using Co-Bi_2MoO_6 as a model photocatalyst, DFT and experimental methods were used to investigate the effect of Co doping for Bi_2MoO_6 photocatalysis. As shown in Fig. 2(b), DFT results showed that Co doping regulates the electronic structure of Co-Bi_2MoO_6, activates Bi sites, and provides a new Co active site, thus constructing a dual active site in Bi_2MoO_6. Electrons were transferred from the d-orbital of Co position (Co-Bi_2MoO_6) to the antibonding orbital to adsorb N_2. Thus, the adsorption/activation properties of N_2 on the surface of transition metal sites (Co and Bi) are depended on electrons, where the electronic structure of the d orbital determines the energy barrier of the nitrogen reduction reaction. UV-vis diffuse reflectance absorption spectroscopy (UV-vis DRS) showed a red shift in the absorption threshold of Co-Bi_2MoO_6, indicating that Co doping expanded the absorption range of Bi_2MoO_6. According to the Tauc curve of the Kubelka–Munk equation, the bandgaps of Bi_2MoO_6 and 3% Co-Bi_2MoO_6 were calculated to be 2.52 and 2.39 eV, respectively. The result showed that Co doping decreased the bandgap to enhance the light absorption. Electrochemical impedance spectroscopy (EIS) results also showed that 3% Co-Bi_2MoO_6 had a better charge separation efficiency than Bi_2MoO_6, which indicated that Co-Bi_2MoO_6 had higher carrier transfer kinetics to carry out satisfactory photocatalysis.

In the process of ion doping, the impurity ions will interact with the lattice atoms of the material, resulting in some lattice atom behaviors. In general, ion doping may lead to lattice atom occupancy or atomic defects, and further affect the photocatalytic activity by affecting the light absorption capacity. Zhang et al. enhanced the photocatalytic activity by doping Fe ions into BiOCl while constructing lattice oxygen vacancy defects.[56] BiOCl nanosheets were synthesized by a hydrothermal method using bismuth chloride ($BiCl_3$) and iron(III) 2,4-glutarate ($Fe(acac)_3$) as precursors, polyethylpyrrolidone as the surfactant

and ethylene glycol as the solvent. By adding a certain amount of $Fe(acac)_3$ to the synthesis process, the 5% doping level of Fe can be easily controlled (Fig. 2(c)). The bandgap of BiOCl NSs-Fe-5% before and after illumination is 3.01 eV and 2.97 eV, respectively, indicating that the introduction of impurities can effectively reduce the band gap to enhance the light absorption. Furthermore, ESR and XPS also demonstrated the presence of oxygen defects after illumination.

In addition to using the cationic doping mode mentioned above, anion doping also affects the band structure of the semiconductor, resulting in changes in light absorption capacity. Xu et al. prepared Br-doped $Bi_2O_2CO_3$ materials by a hydrothermal synthesis method.[57] The results show that doping Br-doped $Bi_2O_2CO_3$ exposed (001) facets can effectively reduce the band gap of $Bi_2O_2CO_3$ by improving the valence band position. As the structure of $Bi_2O_2CO_3$ contains the cationic slabs of $[Bi_2O_2]$ and the anionic slabs, there exists an internal electric field perpendicular to the $[Bi_2O_2]^{2+}$ layer, which can effectively separate the photo-generated carriers. Due to the exposed (001) facets of Br-doped $Bi_2O_2CO_3$, the hole transfer path would be shortened because it would transfer along [001] orientation, facilitating hole transfer to the (001) facets to degrade methyl orange (MO) and rhodamine B (RhB) dyes. Meanwhile, the electrons would migrate to (110) facets to reduce adsorbed O_2 to $•O_2^-$, which can further oxidate MO and/or RhB dyes into small molecules such as CO_2 and H_2O. The photocatalytic properties of degradation of MO and RhB dyes were evaluated by degrading them in aqueous solution. Compared with pure $Bi_2O_2CO_3$, Br-doped $Bi_2O_2CO_3$ showed significantly improved photocatalytic activity, which can be attributed to the enhancement of light absorption capacity after doping with Br ions to promote photogenerated carrier migration and improve the photocatalytic activity.

Reasonable design of different types of ions can effectively change the band structure of the bismuth-based semiconductor photocatalyst, which affects the light absorption capacity and regulates the photocatalytic activity. The doping of impurity ions provides effective guidance for expanding the light absorption and promoting the wide application of bismuth-based photocatalysts.

2.2 Defect engineering

During photocatalytic reactions, the defects of semiconductor materials play an irreplaceable role in influencing the activity. Defects cause the electronic structure and lattice distortion of semiconductor materials, the influence of the electronic structure may be a double-edged sword in adsorption medium molecules, and the change of the electronic structure will cause the change of the molecular atomic orbital and molecular orbital, leading to the change of the properties of semiconductor materials. At the same time, the coordination of defects is unsaturated, which can provide a large number of dangling bonds for preferential adsorption of reactants, and efficient adsorption of reactants is also conducive to charge transfer at the interface. There is also a certain probability that the local electrons at the defect will have electronic feedback to the

adsorbent molecules, thus activating the inert chemical bonds of some adsorbent molecules.[58–61]

Among defect types, oxygen defects are the most widespread because of the wide emergence of oxygen-containing semiconductor materials and the relatively easy construction of surface oxygen vacancies.[62–65] Oxygen vacancies can be used as traps for light-generated electrons, which can show good carrier separation ability. The enrichment of photogenerated electrons is further generated and the light absorption capacity is appropriate in the visible region.[66,67] Hou *et al.* quickly synthesized BiOX/RGO photocatalytic composites rich in oxygen vacancy defects by solvo-free grinding within 15 min. In the synthesis process, the oxygen-containing functional groups on the surface of graphene oxide easily adsorb Bi^{3+} ions. Through electrostatic interactions between ions, negatively charged graphene oxide attracts positively charged metal Bi ions. Subsequently, during the grinding process, BiOX nuclei can be grown

in situ on the graphene oxide to form a more stable heterojunction BiOX/GO compound (Fig. 3(a)). During photocatalysis, oxygen vacancies can lead to a new defect level that increases the absorption of visible light. Therefore, the synergy between heterojunctions and oxygen vacancies guarantees a low tendency for photoinduced carrier recombination to boost the photocatalytic activity.[7] Similarly, inspired by defect engineering and ultra-thin layered material engineering strategies, Li *et al.* synthesized single-layer BiO_{2-x} with abundant vacancies to achieve full spectral response.[68] A comprehensive study of this monolayer material using different diffraction, spectroscopy, microscopy and modeling techniques confirmed the existence of oxygen vacancies. Spectroscopic characterization by DRS showed that the light absorption is 850 nm and 890 nm, which can achieve good near-infrared light absorption (Fig. 3(b)). DFT showed that BiO_{2-x} had semi-metallic properties, which were mainly derived from the valence states of O 2p and Bi 4p.
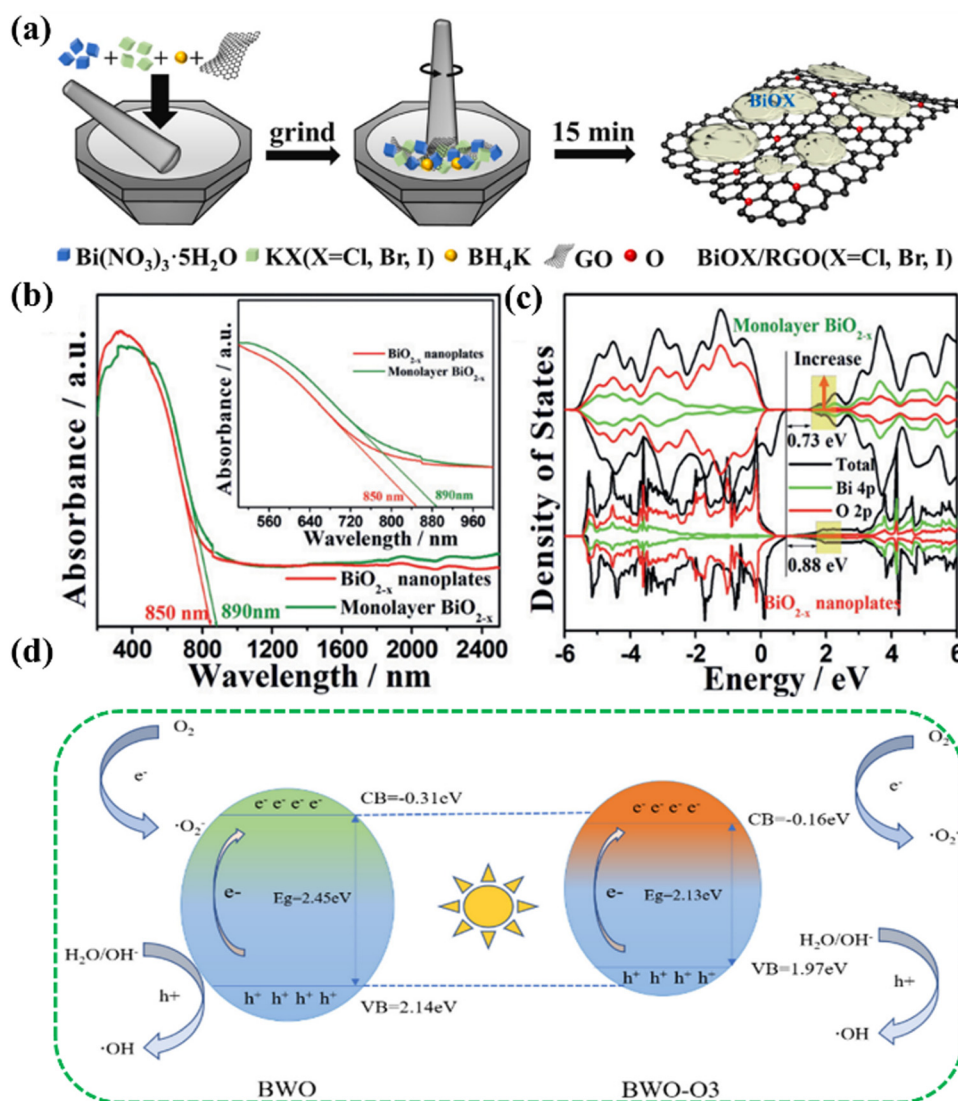

Fig. 3 (a) Synthesis of the BiOX/RGO (X = Cl, Br and I) composite.[6] Copyright 2021, Elsevier. (b) UV/vis-NIR DRS of BiO_{2-x}. (c) Total density of states (TDOS) of BiO_{2-x}.[68] Copyright 2017, Wiley. (d) Schematic of Bi_2WO_6 with/without oxygen vacancies.[69] Copyright 2023, Elsevier.

Table 1 Classification of bismuth-based photocatalysts with different defect types

Photocatalysts	Defect types	Bandgap (eV)	Ref.
Bi_2O_2Se	Se	1.054	70
BiOBr	Bi–Br	2.69	71
$BiPO_4$	Bi–O	—	72
BiOI	I	1.984	73
Bi_2WO_6	Bi	2.42–2.81	74
BiOX	Bi–O	1.56–2.68	75
$Bi_{24}O_{31}Br_{10}$	Bi–O	—	76

And the calculated bandgap are 0.73 eV of monolayer BiO_{2-x} and 0.88 eV of BiO_{2-x} nanoplates, respectively, indicating that they have near-infrared light absorption capacity (Fig. 3(c)). The agreement between the results and experiments indicated that oxygen vacancy defects regulated the light absorption characteristics. Chen et al. fabricated a novel oxygen-vacancy Bi_2WO_6 photocatalytic material by a simple solvothermal method using ethylene glycol and ethanol as solvents.[69] By analyzing the UV-vis DRS of Bi_2WO_6, it can be observed that Bi_2WO_6 with rich oxygen vacancies had a stronger light absorption from 335 to 800 nm, and the visible light absorption range of Bi_2WO_6 achieved a red shift. When oxygen vacancy defects occur, the bandgap of Bi_2WO_6 decreases from 2.45 eV to 2.13 eV. Compared with Bi_2WO_6 with no defects, Bi_2WO_6 with oxygen vacancies had a narrower bandgap and higher photoelectron–hole pair mobility (Fig. 3(d)). The oxygen vacancy enhances the absorption and utilization of visible light, narrowing its bandgap, and lower electrochemical impedance facilitates the separation and transfer efficiency of photogenerated carriers. In addition to the common oxygen vacancy defects, other types of atomic defects are also included. The classification of other vacancy defects in bismuth-based photocatalytic materials is summarized in Table 1.

2.3 Heterojunction

Heterogeneous structure photocatalysts utilize the interface effect between different materials to form a heterogeneous structure. The photoexcited catalyst generates electron–hole pairs, and electrons transfer between different materials through the interface to achieve effective separation of photogenerated carriers.[25] At the same time, efficient light absorption relies on the light absorption capacity of different materials, and then the effective carrier separation and the enhanced light absorption capacity promote the improvement of photocatalytic activity.

In general, heterojunctions are effective couplings of different semiconductors and can be classified into several types: type I (straddling gap), type II (staggered gap), and type III (broken gap) (Fig. 4(a)). For type I, there is a potential discontinuity in the bandgap because the bandgap of one semiconductor is completely superimposed on the other. In type III, however, there is no overlap of bands, and it is difficult to realize the intermigration of electron–hole pairs in Type III heterojunction photocatalysts, making it impossible to facilitate the effective separation and migration, so type III can be regarded as independent semiconductors.[77] Among them, type II

exhibits good charge separation owing to a lower band edge of one semiconductor than the other, and hence electrons are limited to one semiconductor and holes to the other. The photocatalytic activity was improved by enhancing the visible light absorption and carrier kinetics of the photocatalyst.[78] For instance, the $BiOI/Bi_2O_2SO_4$ heterojunction designed by Geng et al., a typical type I heterogeneous structure, exhibits a mismatched band structure between the CB and VB. This type I catalyst $BiOI/Bi_2O_2SO_4$ can realize interfacial charge transfer, activate reactants, and improve photocatalytic activity.[79] The Mott–Schottky slope of BiOI is negative, representing a p-type semiconductor, and the Mott–Schottky slope of $Bi_2O_2SO_4$ is positive, representing an n-type semiconductor. By bringing p-BiOI and n-$Bi_2O_2SO_4$ into contact, electrons can be transferred from n-$Bi_2O_2SO_4$ to p-BiOI until the Fermi level reaches equilibrium, resulting in a positive charge on the n-$Bi_2O_2SO_4$ side of the interface and a negative charge on the p-BiOI side, thus establishing built-in electric field (BEF). Under visible light excitation, photoexcited electrons in BiOI are released and then spontaneously migrate to the CB of $Bi_2O_2SO_4$ driven by the existing BEF, thus effectively accelerating photogenerated charge separation while increasing charge transfer in BiOI (Fig. 4(b)). Zou et al. constructed a lanthanum orthovanadate ($LaVO_4$)/bismuth oxybromide (BiOBr) hybridized heterojunction, as a type II structure, employing a hydrothermal strategy for promoting the separation and transfer efficiency of photogenerated carriers, and achieved photocatalytic air purification.[80] After the coupling of $LaVO_4$ and BiOBr, a heterojunction is formed at the interface of $LaVO_4$ and BiOBr, and the Fermi energy levels of BiOBr and $LaVO_4$ tend to balance, forming an internal electric field. When visible light excites the $LaVO_4$/BiOBr heterojunction, electrons are generated at the CB of $LaVO_4$ and BiOBr, and holes are generated at the VB of $LaVO_4$ and BiOBr. Subsequently, these holes on the VB of BiOBr tend to move to the VB of $LaVO_4$. Furthermore, the excited electrons at the CB of $LaVO_4$ are transferred to the CB of BiOBr. In addition, the internal electric field at the junction interface will further push the holes on the BiOBr VB closer to the holes in $LaVO_4$, while the electrons will move from the CB in $LaVO_4$ to the CB in BiOBr. This type II band alignment can significantly improve the pore separation of accumulated pores and electrons, which can capture adsorbed H_2O to form $OH^•$ participating in photocatalytic oxidation reactions. At the same time, the electrons enriched on the BiOBr CB can react with the adsorbed O_2 to form $O_2^{•-}$, which enhances the photocatalytic activity (Fig. 4(c)). Similarly, Type II heterojunctions also include $BiOBr/SnO_2$,[81] Bi_2O_4–Bi_4O_7–BiO_{2-x},[82] $Bi_2Mo_3O_{12}@Bi_2O_2CO_3$,[83] Bi_2MoO_6/ZnO,[84] etc. The corresponding types of heterojunctions are presented in Table 2.

In addition, metal–semiconductor and organic–semiconductor structural heterojunctions have also been reported for photocatalytic performance optimization.[91,92] Zhang et al. reported surface plasma Ag-decorated Bi_5O_7I microspheres that exhibited excellent light-triggered antibacterial performance for Escherichia coli and Staphylococcus aureus of up to 99.62% and 99.78%, respectively.[93] Under visible light, Bi_5O_7I is excited to produce h^+ and e^-. e^- is easily transferred to biofilm solutions

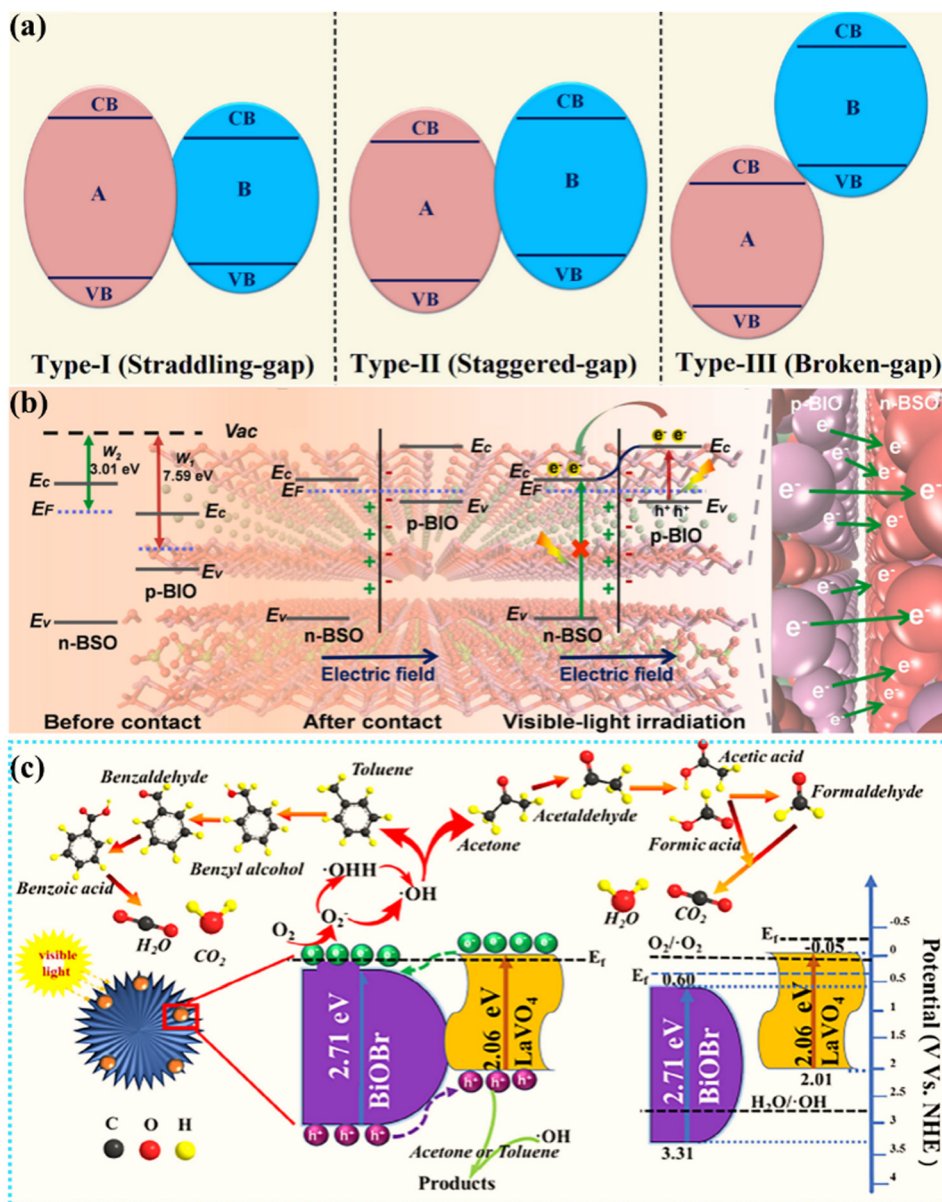**Fig. 4** (a) Schematic of three types of heterojunctions.[78] Copyright 2021, Elsevier. (b) Schematic of the BiOI/Bi$_2$O$_2$SO$_4$ heterojunction.[79] Copyright 2021, Elsevier. (c) Schematic of the bandgap match of 3% LaVO$_4$/BiOBr and the degradation pathway of gaseous acetone or toluene.[80] Copyright 2020, Elsevier.

Table 2 Different types of hybrid photocatalysts

Photocatalysts	Heterojunction types	Ref.
NiO$_x$/Ta$_3$N$_5$	Type II	20
ZnIn$_2$S$_4$/WO$_3$	Type II	85
TiO$_2$–WO$_3$	Type II	86
CuS/Cu$_9$S$_5$	Type II	87
Bi$_2$S$_3$/Ti$_3$C$_2$T$_x$	Type II	88
BiOCl/Bi$_2$O$_3$	Type II	89
BiOI/Bi^0	Type II	90

by Ag particles, facilitating the separation of electron–hole pairs. The transferred e$^-$ not only directly attacks the biofilm, but also reacts with O$_2$ in the water and produces ^{1}O$_2$ and h$^+$, which is captured by H$_2$O and produces •OH. At the same time,

light excitation generates heat, and biological cells in direct contact will be damaged by heat. In addition, Ag$^+$, Bi^{3+} and antifouling groups in the resin can react with mercaptan groups in biofouling organisms and cause protein inactivation, resulting in a breakdown of membrane integrity, leading to more efficient cell deactivation, which provides an effective guidance for highly efficient photothermal catalysis synergistic bacterial inactivation by using metal decorated heterojunctions with surface plasma resonance (SPR). He *et al.* designed Bi quantum dot implanted 2D C-doped BiOCl nanosheets to achieve the enhancement of photocatalytic activity using a hydrothermal method.[94] This work provided a new mechanistic perspective for understanding the synergistic effects of nonmetallic doping and SPR effects in semiconductor photocatalysts, and the technique

can be generalized to other semiconductor materials. Meanwhile, Zhang et al. also reported SPR bismuth enhanced visible photoreactivity of Bi_2WO_6. The enhanced catalytic activity is attributed to interfacial charge separation driven by SPR. The excellent stability of Bi/Bi_2WO_6 demonstrates its potential in photocatalytic pollution treatment applications.[95]

2.4 Morphological construction

Nanomaterials with different scales, structures and morphologies have different light absorption capacities. Compared with spherical materials with three-dimensional structures, nanosheets with two-dimensional structures and more surface unsaturated coordination atoms exposed have a larger surface area and can make better use of light energy.[19,96,97] Meanwhile, two-dimensional materials with atomic thickness and superior physical and chemical properties can shorten the migration distance of photogenerated carriers and improve the efficiency of carrier transfer and separation.[98,99] In addition, the abundant surface unsaturated coordination atoms provide more exposed active sites for interfacial reactions.[42] Ultrasmall nanoparticles, clusters and single atomic structures can achieve an excellent photocatalytic application because of their highly efficient activity and superior specific surface area.[100–105] Di et al.[106] used the atomic layer structure to confine the doping strategy to tune the $Bi_{24}O_{31}Br_{10}$ surface isolated metal sites. They found that the surface isolated Cu can be polarized along the Ci–O–Bi atomic interface, which can better localize the photo-generated electrons, triggering effective N_2 activation. Ou et al. designed PHI nanomaterials modified by Cu single atoms to achieve efficient photocatalytic antibacterial function. Since there are single atoms in the interlayer position of the PHI plane, the interlayer position of PHI can effectively regulate the coordination number, coordination bond length and electronic structure of Cu single atoms, thereby promoting photoinduced electron migration and O_2 activation, thus effectively generating reactive oxygen species (ROS).[107] Zaoming Li also reported single atoms with atomic-level functionalization that have been investigated as next-generation antibacterial materials due to their outstanding stability and biocompatibility resulting from their nitrogen-doped carbon-based nanostructures.[108] Moreover, Baohong Sun anchored Ir and Ru single atoms to improve the light absorption capacity, the broad spectrum of light absorption is extended, and more electron transport is achieved to enhance the catalytic performance.[109] Therefore, changing the size and morphology of the material can achieve more light energy applications and promote photocatalytic activity.

2.5 Facet-orientation engineering

Different atomic crystal facets exhibit different physicochemical properties due to different types of atoms; therefore, facet-oriented engineering can be a favorable way to adjust the surface active sites.[110,111] When different crystal faces are exposed, their surface active atomic effects are strengthened, and they have highly enhanced and stable photocatalytic activity under visible light irradiation.[57] The atoms in different surface exposed facets can lead to different coordination modes and photo-carrier

transfer, which can be used to adjust the surface activity and selectivity of photocatalytic CO_2 reduction.[112] Zhou et al.[113] used a facile room temperature chemical method to synthesize the exposed {001} facet of 2D $Bi_2O_2CO_3$ nanosheets; from this facet, cetyltrimethylammonium bromide (CTAB) can be used as the N source to prepare N-doped $Bi_2O_2CO_3$ for visible light photocatalytic activity study. The 2D $Bi_2O_2CO_3$ nanosheets with the exposed {001} facet have a higher oxygen atomic density and lower Bi–O bond energy, which can provide the surface active sites for grafting with other ions and molecules. Similarly, Wang et al.[114] constructed teethlike BiOCl (001) nanosheets to study their photocatalytic performance. Sun et al.[115] found that in photocatalytic Escherichia coli (E. coli) inactivation, O-defective BiOI with {110} facets can be better than O-defective BiOI with {001} facets because the {110} facets in BiOI with excellent geometric effect obtain strong adsorption capacity for O_2, which can form a high concentration of singlet oxygen species, leading to excellent antibacterial properties. It is confirmed that the adsorption capacity of O_2 is different among different crystal faces, and then the singlet oxygen concentration is different through the free electron interaction, leading to the production of different antibacterial properties. The research of joint facet engineering provided inspiration for the future research of antimicrobial photodynamic therapy. The accumulation of facet-dependent photo-generated charges in one component can manipulate the interfacial charge transfer in heterostructure systems, where the potential difference generated in the interface can also be related to the different crystal facets.[111] Ye et al.[116] fabricated the hetero-surface of {001} (BiOI-001) and {100} (BiOI-100) facets by a hydrothermal method. They found that the self-induced internal electric field is perpendicular to the BiOI-001 nanosheet but parallel to the BiOI-100 nanosheet, which made the separation and transfer of charge in BiO-001 more favorable than in BiO-100 with the internal electric field, and the diffusion distance of the photoinduced charge carriers in BiOI-001 was shorter than that in BiOI-100. The results showed that BiOI-001 had high carrier separation efficiency. Meanwhile, Chen et al.[117] achieved the layered bismuth-based semiconductor (LBB-BiOIO$_3$) crystal facet junction design. As the thickness of $BiOIO_3$ nanoplates decreased along the [010] direction (layer growth direction), the carrier diffusion path was greatly shortened, and at the optimal thickness, the appropriate proportion of $BiOIO_3$ nanoplates exposed {010} and {100} planes can effectively separate photogenerated electrons and holes on the anisotropic plane.

Generally, different modification and treatment methods can obtain very unexpected properties, which provides more possibilities for bismuth-based materials in different applications. Table 3 lists some properties and applications resulting from some corresponding modification methods.

3. Photocatalytic applications

3.1 Degradation

Currently, contaminants in water include antibiotics,[118–122] organic dyes[123–125] and heavy metal ions.[126,127] Photocatalysis

Table 3 Different applications and corresponding modification methods

Photocatalysts	Modifications	Applications	Ref.
$Bi_2Ga_4O_9$	Fe^{3+} doping	Overall water splitting	53
$Bi_2O_2CO_3$	Br-Doped	Degradation of MO and RhB dyes	57
Bi_2WO_6	Bismuth vacancies	Photocatalytic oxygen evolution	59
$H_{1.07}Ti_{1.73}O_4 \cdot H_2O$ nanosheets	Metal defects	Photocatalytic hydrogen evolution	58
BiOCl	Oxygen vacancy	Photocatalytic water oxidation	60
$LaVO_4$/BiOBr	Type II heterojunction	Photocatalytic oxidation reactions	80
Bi_5O_7I	Ag-Decorated	Antibacterial application	93
$Bi_2O_4-Bi_4O_7-BiO_{2-x}$	Type II heterojunction-oxygen vacancy	Photocatalytic degradation	82
$Bi_2O_2CO_3$	{001} facets and N-doped	Photocatalytic degradation	113
BiOCl	O-Defective with {001} facets	Photocatalytic activity	114
BiOI	{110} facets	Photocatalytic *Escherichia coli* (*E. coli*) inactivation	115
BiOI	Hetero-facets {001} and {100}	CO_2 photoreduction	116
$LBB-BiOIO_3$	Facet engineering	CO_2 photoreduction	117

is an effective method for degradation. It works mainly through a photocatalyst to produce photogenerated carriers under light conditions to achieve interaction with water/gas molecules to produce reactive oxygen species free radicals, and to achieve the degradation of organic pollutants through interaction between free radicals and pollutants to destroy the pollutant structure and specific groups. Lin *et al.* synthesized $Bi_4O_5I_2$/GO/$Bi_2Sn_2O_7$ (BI41/1.5GO/BS41) by using a hydrothermal-ultrasonic assisted aqueous precipitation-heat treatment method.[128] As shown in Fig. 5(a), the schematic diagram of the morphology change of the photocatalyst was provided, and BI41/1.5GO/BS41 exhibited a flower-like microsphere structure with an average size of about 8 μm (Fig. 5(b)–(e)). The microstructure of BI41/1.5GO/BS41 was further observed by TEM and HRTEM in Fig. 5(f), and the element composition was collected with EDS in Fig. 5(g). The lattice fringes of BS41 (222) crystal plane are found, and the interplanar spacing is about 0.31 nm, and the presence of Bi, I, Sn, C and O can be observed. The photocatalytic degradation experiment showed that the optimum process conditions of BI41/1.5GO can be further explored. The effects of different initial concentrations of TC-HCl on the photocatalytic activity of BI41/1.5GO/BS41 at lower initial concentrations of BS41 were further studied. When the initial concentration of TC-HCl is less than 15 mg L^{-1}, BI41/1.5GO/BS41 has good photocatalytic activity (Fig. 5(h)). The effect of BI41/1.5GO/BS41 on the photodegradation of TC-HCl was investigated at the initial concentration of 15 mg L^{-1}. The degradation rate of TC-HCl by using BI41/1.5GO/BS41 was gradually increased with the increase of the amount of the catalyst. Adding more BI41/1.5GO/BS41 means that more active sites in the reaction system come into contact with TC-HCl, further increasing the degradation rate. When the catalyst dosage was increased to 0.8 g L^{-1}, the degradation rate of TC-HCl by BI41/1.5GO/BS41 reached 87.53%. This work showed that the BI41/1.5GO/BS41 photocatalyst has important potential in treating domestic sewage contaminated with antibiotics, providing a new solution to solve the contradiction between water purification and energy consumption.

Bismuth oxyhydroxide has good visible light absorption, van der Waals atomic structure to form a built-in electric field to promote carrier migration and other excellent characteristics.

Therefore, Chachvalvutikul *et al.* successfully synthesized $Bi_7O_9I_3$ and $Bi_4O_5Br_2$ photocatalysts by microwave irradiation, which has the advantages of being fast, simple, environmentally friendly and a one-step method. The synthesized photocatalyst was used to degrade organic pollutants. The possible photocatalytic mechanism of the degradation of 4NP by the solid solution photocatalyst was revealed through the reaction material capture experiment, nitro blue tetrazole (NBT) conversion, *o*-aniline oxidation and terylene photoluminescence (TA-PL) detection techniques. The simultaneous photodegradation of selective phenolic compounds with rhodamine B (RhB) dye was also revealed.[129] Fan *et al.* also fabricated a Z-scheme photocatalyst S-BiOBr/$Bi_2Sn_2O_7$ with a 3D/0D interfacial structure to carry out pollutant degradation.[130] As shown in Fig. 6(a), three-dimensional excitation–emission matrix (3D EEM) fluorescence spectroscopy was employed to investigate the degradation behavior of RhB. The photocatalytic efficiency of S-BiOBr/$Bi_2Sn_2O_7$ composites is significantly better than that of BiOBr/$Bi_2Sn_2O_7$ and $Bi_2Sn_2O_7$, which indicates that S doping is an effective strategy to establish new heterojunctions and improve the photocatalytic activity. Within 90 min, 0.01-S-BiOBr/$Bi_2Sn_2O_7$ had the highest degradation activity on RhB, reaching 99.6%, which was 1.35 times that of BiOBr/$Bi_2Sn_2O_7$. Moreover, TC was employed as a pollutant to perform photocatalysis. In order to further reveal the effective degradation of pollutants by the system, a three-dimensional EEM was used to track the dynamic degradation process of TC under different photocatalytic times. The analysis results of UV-visible absorption spectra showed that with the extension of illumination time, the position of the fluorescence center undergoes a slight blue shift along the symmetry axis, which destroys the internal condensed aromatic groups or some special functional groups in the process, and turns large molecules into small molecules (Fig. 6(b)). With the increase of reaction time (Fig. 6(c)), it can be seen that with the increase of irradiation time, the fluorescence intensity of chelates gradually decreases from 20 to 80 min, indicating that the TC structure dissociation or transformation occurs. This work suggested that the novel Z-type heterojunction is a new way to obtain highly efficient photocatalysts and may provide some ideas for difficult antibiotic degradation.
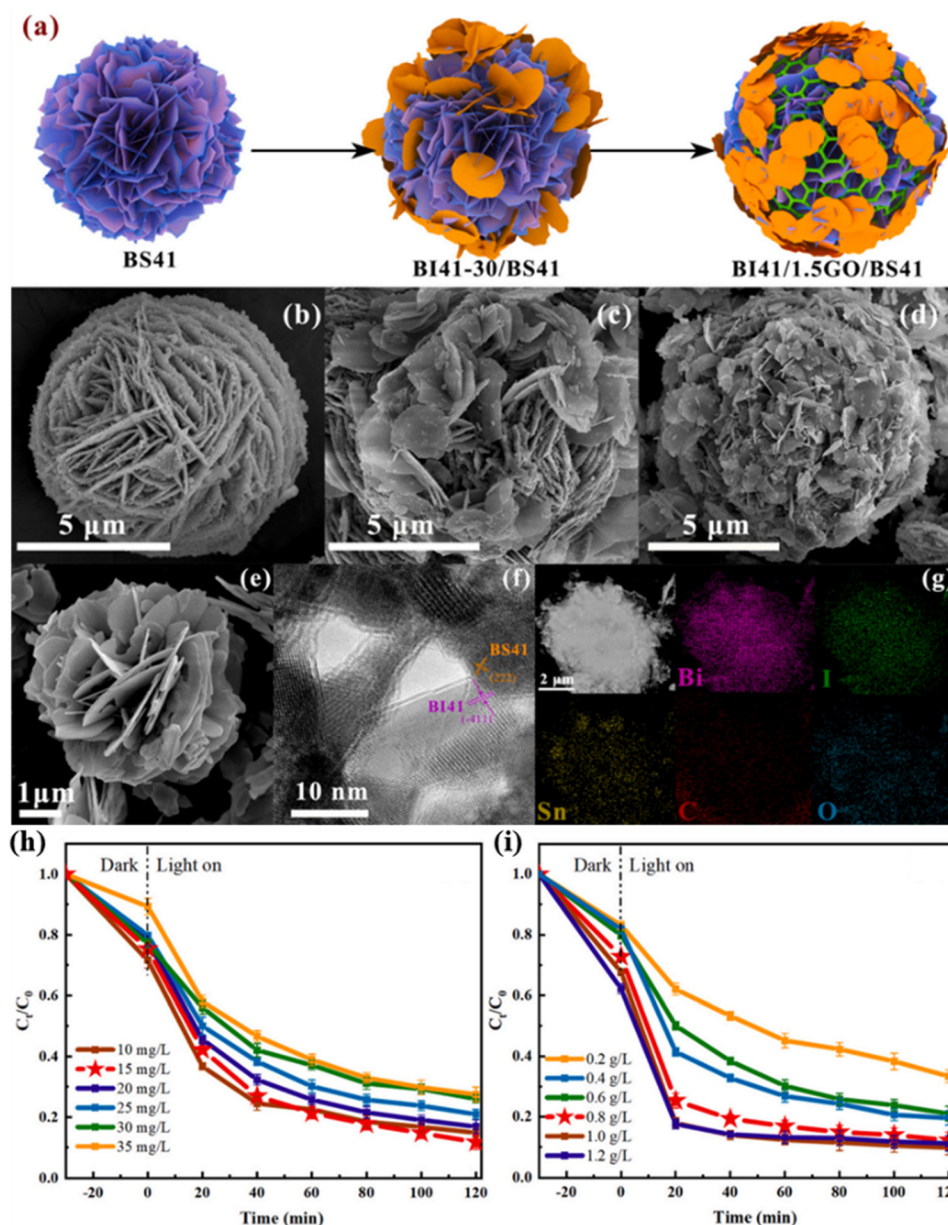
Fig. 5 (a) Schematic of the synthesis process of the BI41/1.5GO/BS41 ternary composite photocatalyst; SEM images of (b) BS41, (c) BI41–30/BS41, and (d) BI41/1.5GO/BS41, and (e) BI41. (f) HRTEM images and (g) element mapping distribution of BI41/1.5GO/BS41. (h) and (i) Degradation curve of TC with different concentrations of BI41/1.5GO/BS41 under illumination.[128] Copyright 2023, Elsevier.

3.2 Energy conversion

Using photocatalysts to realize energy conversion and production is an effective strategy to deal with the current energy crisis. In many photocatalyst energy applications, bismuth-based materials can be used as photocatalysts to achieve CO_2 reduction,[131–134] and water splitting.[135–138] However, the photocatalytic process is controlled by three important continuous steps: (1) light absorption, (2) charge separation and transfer, and (3) surface redox process as shown in Fig. 7.

The construction of bismuth-based photocatalysts in this work provided a new way to improve the activity and stability of photocatalysis. One of the key problems in designing

photocatalysts for CO_2 reduction is to improve the adsorption and activation ability of CO_2 molecules.[21,24,25] To solve this problem, Dai et al. designed α-Bi_2O_3 for high selectivity photocatalytic CO_2 to CH_4 production. In this work, a series of bismuth-based materials with different compositions, structures and morphologies were prepared by adjusting the pH value. The effect of α-Bi_2O_3 on CO_2 and its conversion mechanism was analyzed by DFT (Fig. 8(a)). For pure Bi_2O_3, the carbon atoms of CO_2 molecules are adsorbed at the O position of Bi_2O_3, and the corresponding adsorption energy was −0.173 eV. For Bi–Bi_2O_3, CO_2 is adsorbed through a close interaction between one oxygen atom of CO_2, with a higher adsorption
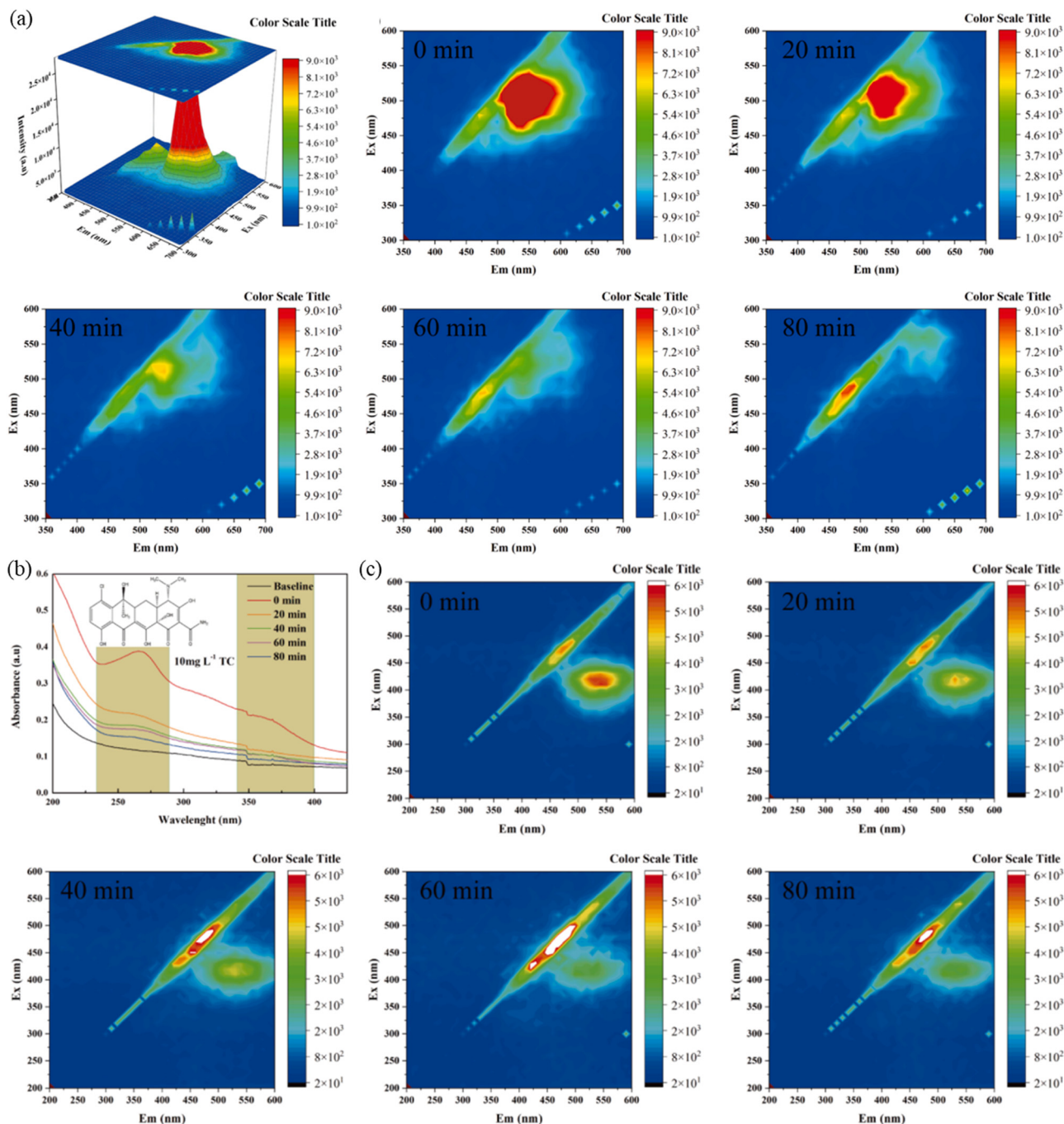
Fig. 6 (a) EEM of RHB before degradation. (b) UV-vis absorption spectra and (c) 3D EEM during the photocatalytic process under irradiation times of 0, 20, 40, 60 and 80 min.[130] Copyright 2023, Elsevier.

energy −0.391 eV. This further showed that the Bi atom of Bi–Bi$_2$O$_3$, as the active site, changed the adsorption configuration of CO$_2$ and greatly improved the adsorption capacity of CO$_2$. It is also worth noting that the C=O bond lengths of CO$_2$ molecules adsorbed on pure Bi$_2$O$_3$ are 1.432 and 1.526, respectively. As shown in Fig. 8(b)–(d), the bond angle for CO$_2$ adsorption decreases from 174.93° on pure Bi$_2$O$_3$ to 159.64° on Bi–Bi$_2$O$_3$. Meanwhile, the O–Bi bond length formed between the adsorption of CO$_2$ and the Bi site by Bi–Bi$_2$O$_3$ is 2.02 Å,

which is also much shorter than the C–O bond length formed between the adsorption of CO$_2$ and the O site by pure Bi$_2$O$_3$ (2.645 Å). Finally, after the active site was converted from O in Bi$_2$O$_3$ to Bi in Bi–Bi$_2$O$_3$, the activation ability of CO$_2$ is significantly enhanced. Furthermore, the interaction of different active sites with CO$_2$ was studied by charge density difference. It can be concluded that the *in situ* preparation of Bi on Bi$_2$O$_3$ is more favorable to the adsorption, activation and hydrogenation of CO$_2$ molecules in the photoreduction process. In addition to

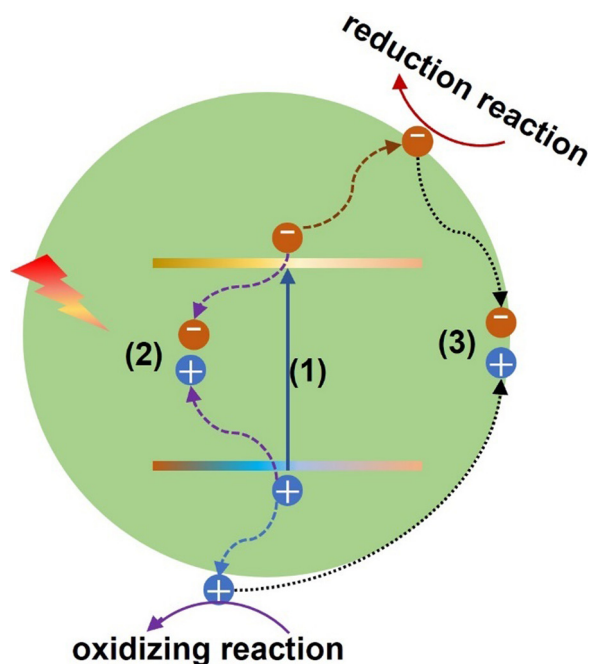Fig. 7 Schematic of the photocatalysis mechanism: (1) light absorption, (2) bulk recombination, and (3) surface recombination.

approach for improving the reduction activity of photocatalysts.[140]

As for water splitting, the band gap should be basically larger than 1.23 eV, and the conduction band is more negative than 0 eV *vs.* NHE, and the valence band should be more positive than 1.23 V *vs.* NHE.[143,144] While, for most Bi-based materials, the conduction band cannot meet the potential of H_2 evolution, some strategies should hence be adopted,[144] especially for the heterojunction. The Z-scheme heterostructure can be the most famous composite for the heterojunction design. Hu *et al.*[145] proposed the facile hierarchical Z-scheme $ZnIn_2S_4/BiCO_4$ heterostructure for photocatalytic H_2 evolution. They could precisely regulate the facile redox center to accelerate the separation and transfer of photo-carriers, thus achieving the productivity of 5.944 mmol g^{-1} h^{-1}, which was five times higher than that of the bare $ZnIn_2S_4$. Yang *et al.*[53] developed loading with RuO_x as a co-catalyst of a $Bi_2Ga_4O_9$ oxide photocatalyst to conduct visible light overall water splitting. With Fe^{3+} to Ga^{3+} substitution, there would appear two adsorption bands at $\sim$731 nm and $\sim$502 nm, because the doped Fe^{3+} cation can strongly bond with O^{2-} ions with the formation of d-p hybrid orbitals, generating two energy levels in the forbidden gap. Therefore, under visible light, electrons can generate from the bonding orbital of $Fe^{3+}-O^{2-}$ to its antibonding orbital to the major conduction band to trigger the water splitting. Furthermore, bismuth-based multimetal oxide photocatalysts of Bi_2WO_6, Bi_2MoO_6, $BiVO_4$, $Bi_4Ti_3O_{12}$, *etc.* were also reported by Zhu *et al.*;[146] they pointed out the future potential and challenges for bismuth-based photocatalysts in the application of water splitting. Similarly, SPR metal Bi-coated $Bi_4O_5Br_2$ (Bi-OVs-$Bi_4O_5Br_2$) photocatalysts were also fabricated by Zhao *et al.* to perform H_2 evolution.[142] The as-prepared Bi-OVs-$Bi_4O_5Br_2$ in this work had excellent photocatalytic activity, and the hydrogen evolution rate was 67.9 µmol g^{-1} h^{-1}, which was 2.1 times that of pure $Bi_4O_5Br_2$. Due to the good heterostructure
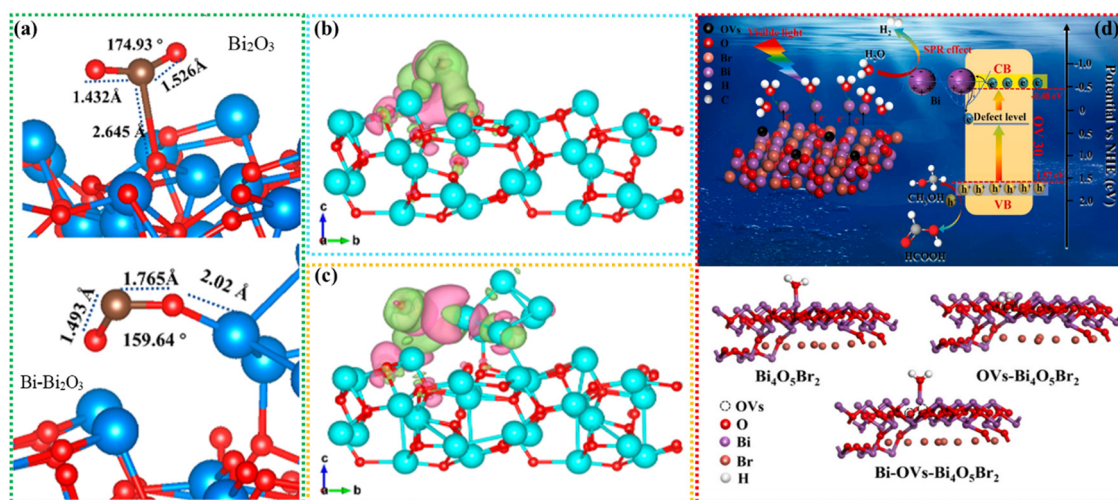
the photogenerated carrier separation, the SPR heterostructure can be used to construct an electric field to promote the carrier separation.[139] At the same time, the broad spectrum response region can be extended by the light absorption characteristics of SPR metals. Thus, Qian *et al.* fabricated Bi/BiOBr to carry out photocatalytic CO_2 reduction. This work showed that the CO and CH_4 yields of the optimal Bi/BiOBr are 251.2 and 25.6 µmol g^{-1} h^{-1}, respectively, which are 12.3 and 8.9 times those of the original BiOBr, indicating that metal deposition on the semiconductor surface can be considered to be an effective

Fig. 8 DFT-designed CO_2 binding structures of (a) pure Bi_2O_3 and Bi–Bi_2O_3. Charge difference distribution of CO_2 adsorbed on (b) pure Bi_2O_3 and (c) Bi–Bi_2O_3. Charge accumulation is given in pink and depletion in green electronic location function.[141] Copyright 2023, American Chemical Society. (d) Schematic of the H_2 evolution mechanism and structure of Bi-OVs-$Bi_4O_5Br_2$.[142] Copyright 2022, Elsevier.

and vacancy defects of SPR, the photocatalytic activity is highly efficient. 2D bismuth-based perovskites ($Cs_3Bi_2X_9$ PNs; X = I, Br, and Cl) designed by Ji et al.[147] were used for H_2 evolution, to promote the electron–hole pair separation, they increased the number of halogen atoms in the octahedral configuration to reduce the distance of Bi–Bi, which can eliminate the strong localization of photo-generated carriers, and therefore, the post-optimized bismuth-based perovskites of $Cs_3Bi_2I_9$ PNs displayed the highest productivity rate of 2157.8 μmol h^{-1} g^{-1} in the H_2 evolution process. Other bismuth-based perovskites for photo-catalytic H_2 evolution received more discussion by Tedesco et al.[148] With surface termination design, Wu et al.[149] found that the structure of 2D Bi_2WO_6 had bilayer Bi_2O_3 sandwiched by WO_4 layers, which can be easily functionalized by some surface termination groups such as Cl^-/Br^- to form Bi–Cl and/or Bi–Br bonds to facilitate photo-carrier separation and narrow its band gap. The results showed that the generation efficiency of H_2 can reach 56.9 μmol g^{-1} h^{-1}.

3.3 Biomedical applications

Bismuth-based nanomaterials, as promising biomedical candidates, were widely explored and employed as contrast agents,[150–153] anti-tumor agents[154–156] and antibacterial agents.[157–159] Wang et al. innovatively designed 2D multifunctional bismuthine for biomedical engineering application.[96]

First, the fabrication of 2D ultra-thin bismuth was carried out by a simple strategy involving two key steps (Fig. 9(a)): (I) a water molecule-mediated freeze–thaw process and (II) $NaBH_4$ reduction treatment. The obtained 2D bismuth showed good optical properties in the near-infrared (NIR) biological window and can be excited by red light to produce reactive oxygen species, enabling applications in a variety of photonic tumor nanomedical fields, including photothermal hyperthermia and photocatalytic therapy. In addition, due to its heavy atomic number, it can be used as a CT contrast agent, and with a photothermal effect, it can be used as a PA contrast agent (Fig. 9(b)). Finally, the integration of diagnosis and treatment will be realized, providing a reliable way for the biomedical application of bismuth-based nanomaterials. Similarly, Cheng et al. fabricated Bi_2S_3 nanorods for the theranostic application for tumor.[160] Bi_2S_3 nanorods prolonged the neutral blood circulation time due to their special size and facilitated tumor accumulation by enhancing permeability and retention (EPR). The acidic tumor microenvironment (pH 6.5) changes the surface charge of Bi_2S_3 from negative to positive, promoting its internalization into tumor cells, and then endolysosome escape. In the cytoplasm, HO-1 captured by the zinc protoporphyrin IX segment of Bi_2S_3 showed weaker antioxidant defenses. Under the irradiation of an 808 nm laser, Bi_2S_3 showed photothermal effect,[156] and the generated heat can
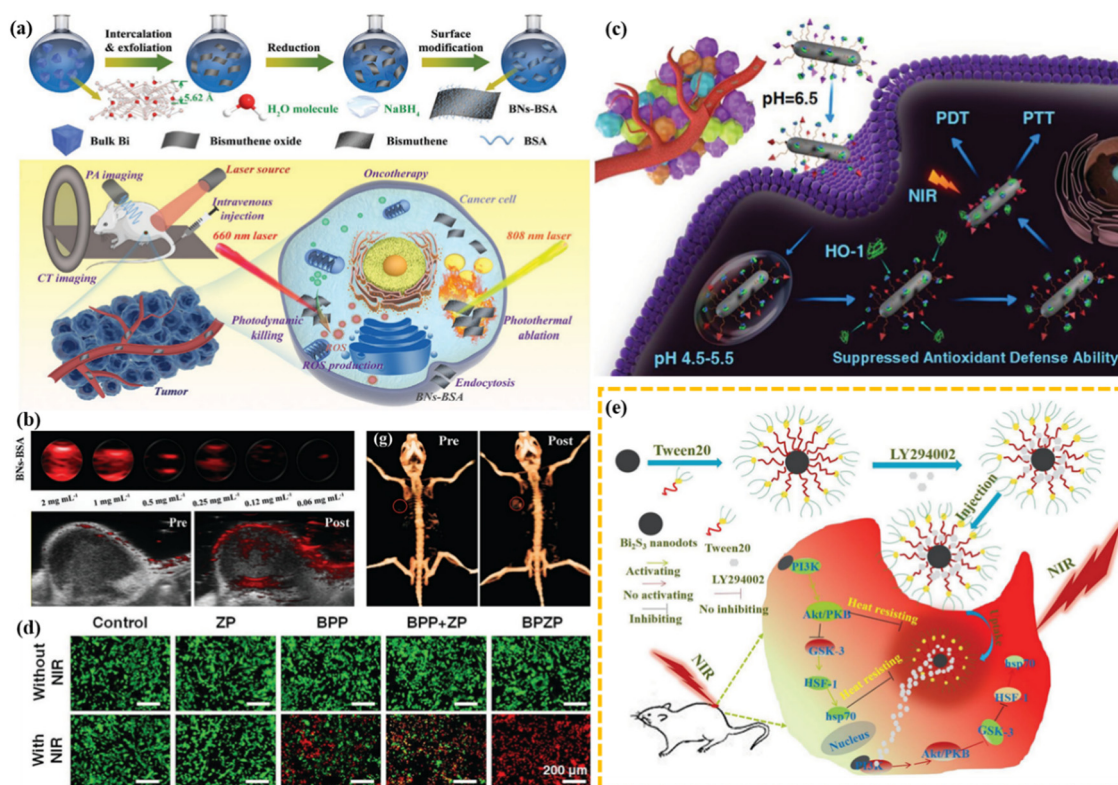

Fig. 9 (a) Schematic of the synthetic procedure and PA/CT/anti-tumor applications of 2D multifunctional bismuthine. (b) CT/PA imaging of bismuthine.[96] Copyright 2021 Wiley. (c) Schematic of the therapeutic mechanism of BPZP through suppressing HO-1 activity and promoting the introduction of NIR laser-triggered ROS. (d) Dead/live cell staining of cells treated with ZP, BPP, BPP + ZP, and BPZP.[160] Copyright 2019, Wiley. (e) Bi_2S_3-Tween 20 nanodots for tumor synergistic therapy.[156] Copyright 2018, Wiley.
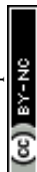
shrink the zinc protoporphyrin IX fragment to produce ROS to kill the tumors (Fig. 9(c)). The effect of NIR-driven therapy of Bi_2S_3 can be further confirmed by live cell/dead cell staining (Fig. 9(d)). Meanwhile, the photothermal effect caused by Bi_2S_3 under NIR irradiation can assist the death of cells and achieve the therapeutic effect on tumor (Fig. 9(e)). In summary, the Bi_2S_3 nanoplatform aims to provide an effective guidance for CT-image-guided photothermal and photocatalytic therapy of tumors.

Bacterial infections are one of the leading causes of death worldwide, posing a long-term threat to public health and placing a heavy burden on healthcare systems. In order to deal with the serious problems caused by bacterial infections and reduce the production of drug-resistant bacteria, the use of bismuth-based photocatalysts to achieve antimicrobial therapy has brought benefits for the treatment of infectious diseases. Considering the good optical properties, and relatively safe and non-toxic nature of bismuth oxyhalide, it can be employed as an effective candidate material for anti-infection therapy. Hence, Kong et al. prepared BiOI nanoparticles functionalized with polydopamine (PDA) and glycol chitosan (GCS) to promote diabetic wound healing (Fig. 10(a)), called $BiO_{1-x}I@PDA@GCS$ (GPBO).[30] In this work, $BiO_{1-x}I$ had photothermal and photocatalytic properties, which is designed as the core of

the material. The author cleverly performed PDA coating as the shell to enhance the photothermal conversion of $BiO_{1-x}I$. The morphology of BO ($BiO_{1-x}I$), PBO ($BiO_{1-x}I@PDA$) and GPBO was obtained by using SEM (Fig. 10(b)). The results show that BO has regular flower-like nanostructures. The prepared PBO and GPBO showed a similar morphology to BO, and the average sizes of BO, PBO and GPBO were 350 nm, 400 nm and 450 nm, respectively. The surfaces of PBO and GPBO were smoother than that of BO. Subsequently, the broad-spectrum antibacterial activity of BO, PBO and GPBO on P. aeruginosa, S. aureus and E. coli was estimated by the plate culture method. As shown in Fig. 10(c), the results showed that under the condition of equivalent concentration of 500 μg mL^{-1}, combined with 808 nm laser irradiation, all the materials showed good antibacterial effect. In particular, the light elimination efficiency of GPBO for various bacteria is nearly 100%. For wound treatment, the wound size decreased over time in all treatment groups (Fig. 10(d)). Good results indicated that in the diabetic wound model, antibacterial and anti-inflammatory GPBO promoted the healing of diabetic wounds. Multifunctional GPBO assisted by NIR was a safe and effective treatment strategy for diabetic wounds and offered a potential solution for the treatment of associated infectious diseases.
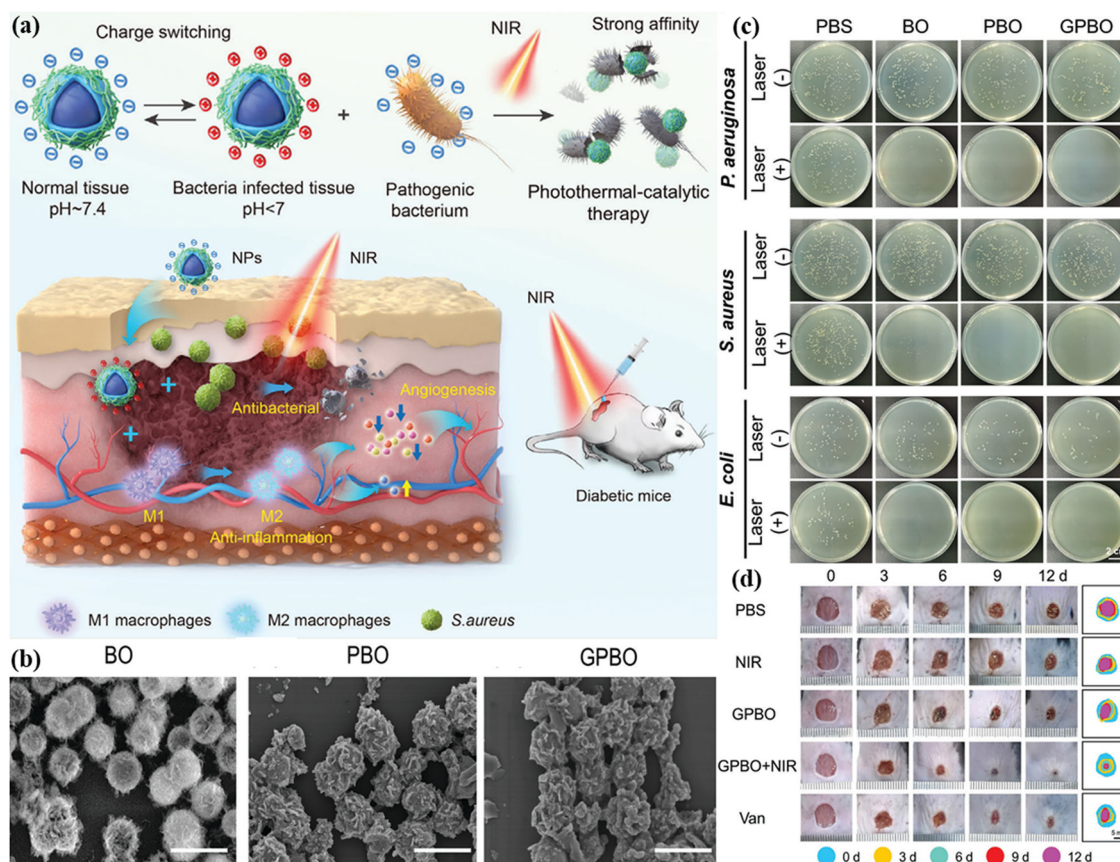

Fig. 10 (a) Schematic of GPBO for the acceleration of wound healing in the diabetic mouse model. (b) SEM images of BO, PBO and GPBO. (c) Photographs and quantitative analysis of the bacterial colonies after the treatments of PBS, BO, PBO, and GPBO at pH 6.5 with or without 808 nm laser irradiation. (d) Photographs of the wound area after different treatments from day 0 to day 12.[30] Copyright 2024 Wiley.
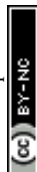
4. Conclusion and outlook

As a rising star in the field of photocatalysis, bismuth-based photocatalysts have attracted extensive attention in recent years due to their unique advantages such as abundant reserves, low preparation cost, suitable electron band structure and reduced toxicity. Although bismuth-based photocatalysts have been developed rapidly, they still cannot meet the requirements of practical applications. Therefore, it is expected to improve the photocatalytic activity of bismuth-based photocatalysts by effective means to achieve the greatest potential applications in different fields. In this review, we summarized the photocatalytic performance improvement strategies of bismuth-based photocatalysts in detail, and summarized their application in different fields, hoping that researchers in different fields can better understand the excellent characteristics of bismuth-based photocatalysts to promote the development of photocatalysts and achieve a broader field of application.

Although the efforts of scientists have developed a wide range of bismuth-based photocatalyst modification strategies and made some breakthroughs, the stability and safety of existing bismuth-based photocatalysts, such as light energy utilization efficiency, production efficiency, catalytic activity, *etc.*, still cannot meet the needs of industrial production; especially, the commercial application of research results in antimicrobial treatment, CO_2 reduction and pollutant degradation is still weak. Therefore, we must continue to seek breakthroughs in the following areas:

Firstly, compared with antibiotics, the antimicrobial mechanism of photoinitiation by nano-photocatalysts is still unclear. According to a large amount of evidence, most bismuth-based materials cannot undergo plastic cell internalization, and kill bacteria mainly through oxidative damage, mechanical stress damage and thermal membrane damage. Therefore, standardized application in antimicrobial of nano-photocatalysts are limited. At the same time, during the preparation process, the repeatability of bismuth-based nanomaterials is low, and the biosafety of bismuth-based nanomaterials is an important key factor in clinical application. The research reports on bismuth-based nanomaterials are relatively scarce, which limits their industrial production.

Secondly, during photocatalytic CO_2 conversion, the reported activity of bismuth-based photocatalysts is generally low, and it is necessary to further improve the activity of catalysts to improve the efficiency of photocatalytic CO_2 reduction and the selectivity of products. The photocatalyst is easy to be deactivated or decomposed during the reaction, which leads to the poor stability of the catalyst, so it is necessary to find a more stable photocatalyst by appropriate methods. In terms of products, bismuth-based photocatalyst products are diverse, and how to effectively control the selectivity of products is a challenge. Photoreduction of CO_2 or photolysis of water splitting involves the efficient usage and transport of photogenerated electrons. Therefore, based on the subsequent study of bismuth-based materials, in-depth studies should be considered from the perspective of thermodynamics and dynamics, such as the regulation of the band structure of bismuth-based materials through tuning the number of layers or atomic ratio, and thus the effective potential can be regulated from the perspective of thermodynamics. In addition, in the transport process of photogenerated carriers, the realization of an effective transport channel is a prerequisite for the effective aggregation of photoelectrons, so that multiple electrons can be better aggregated, which can drive the photocatalytic reduction of CO_2 or improve the performance of photolysis water splitting.

Moreover, for the photocatalytic degradation section, regardless of the low utilization efficiency of photogenerated carriers, resulting in insufficient photocatalytic degradation activity and long irradiation time, the recycling of the photocatalyst is also a big problem. In most studies, the photocatalyst mainly exists in the form of powder, and how to effectively recycle it is an urgent problem to be solved. In addition, the environmental toxicity of photocatalysts also needs to be carefully assessed, as it is important to assess the safety of catalysts in water bodies or the atmosphere that may enter the biosphere cycle and then be absorbed by organisms.

Conflicts of interest

The authors declare no conflict of interest.

Acknowledgements

References

1 A. Hussain, J. Hou, M. Tahir, S. S. Ali, Z. U. Rehman, M. Bilal, T. Zhang, Q. Dou and X. Wang, *Catal. Rev. Sci. Eng.*, 2022, **66**, 119–173.

2 B. Wang, G. M. Biesold, M. Zhang and Z. Lin, *Chem. Soc. Rev.*, 2021, **50**(12), 6914.

3 H. Wu, L. Li, S. Wang, N. Zhu, Z. Li, L. Zhao and Y. Wang, *Phys. Chem. Chem. Phys.*, 2023, **25**, 25899–25924.

4 C. Chen, T. Jiang, J. Hou, T. Zhang, G. Zhang, Y. Zhang and X. Wang, *J. Mater. Sci. Technol.*, 2022, **114**, 240–248.

5 T. Yang, E. Zhu, H. Guo, J. Du, Y. Wu, C. Liu and G. Che, *ACS Appl. Mater. Interfaces*, 2021, **13**(43), 51447–51458.

6 J. Hou, T. Zhang, T. Jiang, X. Wu, Y. Zhang, M. Tahir, A. Hussain, M. Luo, J. Zou and X. Wang, *J. Cleaner Prod.*, 2021, **328**, 129651.

7 J. Hou, T. Jiang, X. Wang, G. Zhang, J.-J. Zou and C. Cao, *J. Cleaner Prod.*, 2021, **287**, 125072.

8 G. J. Lee, Y. C. Zheng and J. J. Wu, *Catal. Today*, 2018, **307**, 197–204.

9 J. Ke, J. Liu, H. Sun, H. Zhang, X. Duan, P. Liang, X. Li, M. O. Tade, S. Liu and S. Wang, *Appl. Catal., B*, 2017, **200**, 47–55.

10 H. Fujito, H. Kunioku, D. Kato, H. Suzuki, M. Higashi, H. Kageyama and R. Abe, *J. Am. Chem. Soc.*, 2016, **138**, 2082–2085.

11 Y. Shi, L. Li, Z. Xu, F. Guo and W. Shi, *Chem. Eng. J.*, 2023, **459**, 141549.

12 K. B. Jiang, W. Q. Huang, T. T. Song, P. X. Wu, W. F. Wang, Q. S. Chen, M. S. Wang and G. C. Guo, *Adv. Funct. Mater.*, 2023, **33**(43), 2304351.

13 S. Liu, X. Guo, W. Wang, Y. Yang, C. Zhu, C. Li, W. Lin, Q. Tian and Y. Liu, *Appl. Catal., B*, 2022, **303**, 120909.

14 Z. Lian, F. Wu, Y. Zhong, J. Zi, Z. Li, X. Wang, T. Nakagawa, H. Li and M. Sakamoto, *Appl. Catal., B*, 2022, **318**, 121860.

15 J. Yang, H. Su, Y. Wu, D. Li, D. Zhang, H. Sun and S. Yin, *Chem. Eng. J.*, 2021, **420**, 127607.

16 B. Xiao, T. Lv, J. Zhao, Q. Rong, H. Zhang, H. Wei, J. He, J. Zhang, Y. Zhang, Y. Peng and Q. Liu, *ACS Catal.*, 2021, **11**(21), 13255.

17 H. Bai, S. H. Lam, J. Yang, X. Cheng, S. Li, R. Jiang, L. Shao and J. Wang, *Adv. Mater.*, 2021, **34**, 2104226.

18 Y. W. Wang, X. S. Hu, H. R. Song, Y. Cai, Z. Li, D. Y. Zu, P. X. Zhang, D. T. Chong, N. B. Gao, Y. M. Shen and C. P. Li, *Appl. Catal., B*, 2021, **299**, 120677.

19 L. Zhu, Y. Wu, S. Wu, F. Dong, J. Xia and B. Jiang, *ACS Appl. Mater. Interfaces*, 2021, **13**(7), 9216.

20 L. Pei, X. Wang, H. Zhu, H. Yu, S. Bandaru, S. Yan and Z. Zou, *ACS Appl. Mater. Interfaces*, 2023, **15**(44), 51300.

21 D. Long, J. Liu, H. Chen, P. Liu, K. Zheng, Y. Zeng, X. Chen, S. Li and M. Lu, *Appl. Catal., B*, 2023, **330**, 122625.

22 X. Shi, X. a Dong, Y. He, P. Yan, S. Zhang and F. Dong, *ACS Catal.*, 2022, **12**(7), 3965.

23 Y. Xi, X. Zhang, Y. Shen, W. Dong, Z. Fan, K. Wang, S. Zhong and S. Bai, *Appl. Catal., B*, 2021, **297**, 120411.

24 D. Long, J. Peng, H. Liu, Z. Feng, L. Chen, X. Chen and M. Lu, *Sol. Energy Mater. Sol. Cells*, 2020, **209**, 110446.

25 D. Long, J. Liu, L. Bai, L. Yan, H. Liu, Z. Feng, L. Zheng, X. Chen, S. Li and M. Lu, *ACS Photonics*, 2020, **7**(12), 3394–3400.

26 Y. Wang, Y. Liu, L. Tan, X. Lin, Y. Fang, X. F. Lu, Y. Hou, G. Zhang and S. Wang, *J. Mater. Chem. A*, 2023, **11**, 26804–26811.

27 B. Su, Y. Kong, S. Wang, S. Zuo, W. Lin, Y. Fang, Y. Hou, G. Zhang, H. Zhang and X. Wang, *J. Am. Chem. Soc.*, 2023, **145**, 27415–27423.

28 Y. Liu, W. Xue, X. Liu, F. Wei, X. Lin, X. F. Lu, W. Lin, Y. Hou, G. Zhang and S. Wang, *Small*, 2024, 2402004.

29 W. Guo, W. Shi, J. Cai, F. Wei, X. Lin, X. Lu, Z. Ding, Y. Hou, G. Zhang and S. Wang, *Catal. Sci. Technol.*, 2024, **14**, 2921–2928.

30 J. Kong, S. Ma, R. Chu, J. Liu, H. Yu, M. Mao, X. Ge, Y. Sun and Y. Wang, *Adv. Mater.*, 2024, 2307695.

31 S. Ma, Y. Li, X. Luo, S. Zhao, Z. Cao, Y. Ding, D. Cui, N. Zhou, L. Wang and G. Ran, *Mater. Today Energy*, 2023, **31**, 101214.

32 R. Ghosh, A. Baut, G. Belleri, M. Kappl, H.-J. Butt and T. M. Schutzius, *Nat. Sustain.*, 2023, **6**, 1663–1672.

33 Z. Chen, D. Yang, Z. Liang, Y. Xu, Y. Pang, G. Xu, C. Chen, K. Ma, L. Zhou and B. Yan, *Chem. Eng. J.*, 2023, **474**, 145978.

34 X. Zhang, F. Tian, X. Lan, Y. Liu, W. Yang, J. Zhang and Y. Yu, *Chem. Eng. J.*, 2022, **429**, 132588.

35 S. Ma, J. Kong, X. Luo, J. Xie, Z. Zhou and X. Bai, *Sci. Total Environ.*, 2024, **915**, 170125.

36 S. Ma, J. Xie, L. Wang, Z. Zhou, X. Luo, J. Yan and G. Ran, *ACS Appl. Mater. Interfaces*, 2021, **13**, 10728–10740.

37 S. Ma, L. Wang, Z. Liu, X. Luo, Z. Zhou, J. Xie, Y. Li, S. Cong, M. Zhou, Y. Xu and G. Ran, *Nanoscale*, 2021, **13**, 185–194.

38 M. Yuan, S. Xu, Q. Zhang, B. Zhao, B. Feng, K. Ji, L. Yu, W. Chen, M. Hou, Y. Xu and X. Fu, *Chem. Eng. J.*, 2020, **394**, 124874.

39 N. Yang, W. Xiao, X. Song, W. Wang and X. Dong, *Nano-Micro Lett.*, 2020, **12**, 1–27.

40 Y. Song, L. Yang, M. Xu, Q. Lu, W. Li, C. Ren, P. Liu, Y. Wang, Y. Zhu, F. Tan and N. Li, *Biomater.*, 2020, **254**, 120140.

41 L. Zhang, Y. H. Li, Q. Li, J. J. Fan, S. A. C. Carabineiro and K. L. Lv, *Chem. Eng. J.*, 2021, **419**, 129484.

42 H. Ma, Y. He, P. Chen, H. Wang, Y. J. Sun, J. Y. Li, F. Dong, G. X. Xie and J. P. Sheng, *Chem. Eng. J.*, 2021, **417**, 129305.

43 X. Tao, X. Zhou and R. Li, *Chem. Commun.*, 2024, **60**, 5136–5148.

44 P. Muthukumar Sathya, S. Vadivel, T. Shin and H. Mohan, *Inorg. Chem. Commun.*, 2022, **144**, 109924.

45 X. Wang, Y. Wang, M. Gao, J. Shen, X. Pu, Z. Zhang, H. Lin and X. Wang, *Appl. Catal., B*, 2020, **270**, 118876.

46 J. Di, X. Zhao, C. Lian, M. Ji, J. Xia, J. Xiong, W. Zhou, X. Cao, Y. She, H. Liu, K. P. Loh, S. J. Pennycook, H. Li and Z. Liu, *Nano Energy*, 2019, **61**, 54–59.

47 P. Wang, P. Yang, Y. Bai, T. Chen, X. Shi, L. Ye and X. Zhang, *J. Taiwan Inst. Chem. Eng.*, 2016, **68**, 295–300.

48 H. W. Huang, C. Zhou, X. C. Jiao, H. F. Yuan, J. W. Zhao, C. Q. He, J. Hofkens, M. B. J. Roeffaers, J. L. Long and J. A. Steele, *ACS Catal.*, 2020, **10**, 1439–1443.

49 S. Ma, X. Luo, G. Ran, Y. Li, Z. Cao, X. Liu, G. Chen, J. Yan and L. Wang, *Chem. Eng. J.*, 2022, **435**, 134810.

50 B.-J. Ng, L. K. Putri, X. Y. Kong, K. P. Y. Shak, P. Pasbakhsh, S.-P. Chai and A. R. Mohamed, *Appl. Catal., B*, 2018, **224**, 360–367.

51 L. Tan, C. Nie, Z. Ao, H. Sun, T. An and S. Wang, *J. Mater. Chem. A*, 2020, **9**, 17–33.

52 P. Liu, H. Chen, C. Zhao, D. Long, W. Chen, M. Lu and X. Chen, *Appl. Surf. Sci.*, 2024, **659**, 159887.

53 J. Yang, P. Jiang, M. Yue, D. Yang, R. Cong, W. Gao and T. Yang, *J. Catal.*, 2017, **345**, 236–244.

54 J. F. Wang, C. R. Zhao, S. D. Yuan, X. J. Li, J. Y. Zhang, X. Hu, H. J. Lin, Y. Wu and Y. M. He, *J. Colloid Interface Sci.*, 2023, **638**, 427–438.

55 C. M. Yang, Y. Y. Zhang, F. Yue, R. Du, T. X. Ma, Y. J. Bian, R. Q. Li, L. Guo, D. J. Wang and F. Fu, *Appl. Catal., B*, 2023, **338**, 123057.

56 N. Zhang, L. G. Li, Q. Shao, T. Zhu, X. Q. Huang and X. H. Xiao, *ACS Appl. Energy Mater.*, 2019, **2**, 8394–8398.

57 J. Xu, K. K. Wang, T. Liu, Y. Peng and B. G. Xu, *CrystEngComm*, 2017, **19**, 5001–5007.

58 Y. Song, H. Wang, J. Xiong, B. Guo, S. Liang and L. Wu, *Appl. Catal., B*, 2018, **221**, 473–481.

59 J. Di, C. Chen, C. Zhu, M. Ji, J. Xia, C. Yan, W. Hao, S. Li, H. Li and Z. Liu, *Appl. Catal., B*, 2018, **238**, 119–125.

60 H. Li, J. Shang, H. Zhu, Z. Yang, Z. Ai and L. Zhang, *ACS Catal.*, 2016, **6**, 8276–8285.

61 H. Chen, L. Wang, D. Long, Y. Zeng, S. Jiang, W. Chen, C. Zhao, C. Cheng, Y. Chen, M. Lu, S. Li and X. Chen, *Appl. Catal., B*, 2024, **357**, 124260.

62 C. Cheng, D. Y. Chen, N. J. Li, H. Li, Q. F. Xu, J. H. He and J. M. Lu, *J. Colloid Interface Sci.*, 2022, **609**, 447–455.

63 X. Xiao, S. Yang, T. E and Y. Li, *Mater. Today Chem.*, 2023, **27**, 101281.

64 S. Wei, H. X. Zhong, H. T. Wang, Y. J. Song, C. M. Jia, M. Anpo and L. Wu, *Appl. Catal., B*, 2022, **305**, 110413.

65 T. Shi, H. L. Jia, Y. M. Feng, B. Gong, D. M. Chen, Y. Liang, H. Ding, K. Chen and D. R. Hao, *Front. Chem. Sci. Eng.*, 2023, **17**, 1937–1948.

66 G. Li, W. Y. Yang, S. Gao, Q. Q. Shen, J. B. Xue, K. X. Chen and Q. Li, *Chem. Eng. J.*, 2021, **404**, 127115.

67 C. Lu, X. Li, Q. Wu, J. Li, L. Wen, Y. Dai, B. Huang, B. Li and Z. Lou, *ACS Nano*, 2021, **15**, 3529–3539.

68 J. Li, X. Wu, W. Pan, G. Zhang and H. Chen, *Angew. Chem., Int. Ed.*, 2018, **57**, 491–495.

69 L. L. Chen, B. Xu, M. M. Jin, L. J. Chen, G. Y. Yi, B. L. Xing, Y. L. Zhang, Y. F. Wu and Z. H. Li, *J. Mol. Struct.*, 2023, **1278**, 134911.

70 S. W. Han, W. S. Yun, S. Seong, Z. Tahir, Y. S. Kim, M. Ko, S. Ryu, J. S. Bae, C. W. Ahn and J. Kang, *J. Phys. Chem. Lett.*, 2024, **15**, 1590–1595.

71 B. Yang, W. J. Wang, Z. Z. Hu, B. X. Shen and S. Q. Guo, *J. Hazard. Mater.*, 2023, **458**, 132008.

72 H. C. Zheng, J. C. Wang, B. Kong, X. Xu, M. Zhang and W. T. Wang, *Phys. Chem. Chem. Phys.*, 2023, **25**, 30848–30857.

73 X. W. Wang, C. X. Zhou, L. C. Yin, R. B. Zhang and G. Liu, *ACS Sustainable Chem. Eng.*, 2019, **7**, 7900–7907.

74 Z. H. Kang, E. Z. Lin, N. Qin, J. Wu and D. H. Bao, *ACS Appl. Mater. Interfaces*, 2022, **14**, 11375–11387.

75 H. N. Fernández-Escamilla, J. I. Paez-Ornelas, C. D. Gutiérrez-Lazos, F. J. Solís-Pomar, J. Guerrero-Sánchez and E. G. Pérez-Tijerina, *Appl. Surf. Sci.*, 2023, **618**, 156583.

76 J. Di, C. Chen, C. Zhu, R. Long, H. L. Chen, X. Z. Cao, J. Xiong, Y. X. Weng, L. Song, S. Z. Li, H. M. Li, Y. J. Xiong and Z. Liu, *Adv. Energy Mater.*, 2021, **11**, 2102389.

77 J. Low, J. Yu, M. Jaroniec, S. Wageh and A. A. Al-Ghamdi, *Adv. Mater.*, 2017, **29**, 1601694.

78 R. Kumar, P. Raizada, N. Verma, A. Hosseini-Bandegharaei, V. K. Thakur, Q. V. Le, V. H. Nguyen, R. Selvasembian and P. Singh, *J. Cleaner Prod.*, 2021, **297**, 126617.

79 Q. Geng, H. Xie, Y. He, Y. Sun, X. Hou, W. Zhiming and F. Dong, *Appl. Catal., B*, 2021, **297**, 120492.

80 X. J. Zou, C. Y. Yuan, Y. Y. Dong, H. Ge, J. Ke and Y. B. Cui, *Chem. Eng. J.*, 2020, **379**, 122380.

81 H. Wu, C. Yuan, R. Chen, J. Wang, F. Dong, J. Li and Y. Sun, *ACS Appl. Mater. Interfaces*, 2020, **12**, 43741–43749.

82 Y. Jia, S. Li, H. Ma, J. Gao, G. Zhu, F. Zhang, J. Y. Park, S. Cha, J. S. Bae and C. Liu, *J. Hazard. Mater.*, 2020, **382**, 121121.

83 W. C. Huo, T. Cao, W. N. Xu, Z. Y. Guo, X. Y. Liu, H. C. Yao, Y. X. Zhang and F. Dong, *Chin. J. Catal.*, 2020, **41**, 268–275.

84 G. P. Zhang, D. Y. Chen, N. J. Li, Q. F. Xu, H. Li, J. H. He and J. M. Lu, *Appl. Catal., B*, 2019, **250**, 313–324.

85 Y. Wang, W. Huang, S. Guo, X. Xin, Y. Zhang, P. Guo, S. Tang and X. Li, *Adv. Energy Mater.*, 2021, **11**, 2102452.

86 L. Kang, X. Y. Liu, A. Wang, L. Li, Y. Ren, X. Li, X. Pan, Y. Li, X. Zong, H. Liu, A. I. Frenkel and T. Zhang, *Angew. Chem., Int. Ed.*, 2020, **59**, 12909–12916.

87 Z. Zhang, J. Sun, S. Mo, J. Kim, D. Guo, J. Ju, Q. Yu and M. Liu, *Chem. Eng. J.*, 2022, **431**, 134287.

88 J. Li, Z. Li, X. Liu, C. Li, Y. Zheng, K. W. K. Yeung, Z. Cui, Y. Liang, S. Zhu, W. Hu, Y. Qi, T. Zhang, X. Wang and S. Wu, *Nat. Commun.*, 2021, **12**, 1224.

89 C. Su, M. Cheng, H. Gao, J. Li and R. Chen, *Sep. Purif. Technol.*, 2024, **336**, 126229.

90 C. T. Haile, K. H. Ng, C.-W. Chiu, N. Ahmad and C.-F. J. Kuo, *Mater. Today Phys.*, 2024, **42**, 101352.

91 S. Ma, J. Kong, X. Luo, J. Xie, Z. Zhou and X. Bai, *Sep. Purif. Technol.*, 2024, **341**, 126932.

92 S. Ma, X. Luo, J. Kong, X. Li, Z. Cao, X. Wang, W. Cai, L. Wang and G. Ran, *Chem. Eng. J.*, 2022, **450**, 138016.

93 L. L. Zhang, J. N. Sha, R. R. Chen, Q. Liu, J. Y. Liu, J. Yu, H. S. Zhang, C. G. Lin, W. Zhou and J. Wang, *Appl. Catal., B*, 2020, **271**, 118920.

94 Y. He, J. Y. Li, K. L. Li, M. L. Sun, C. W. Yuan, R. M. Chen, J. P. Sheng, G. Leng and F. Dong, *Chin. J. Catal.*, 2020, **41**, 1430–1438.

95 L. Zhang, C. Yang, K. L. Lv, Y. C. Lu, Q. Li, X. F. Wu, Y. H. Li, X. F. Li, J. J. Fan and M. Li, *Chin. J. Catal.*, 2019, **40**, 755–764.

96 Y. M. Wang, W. Feng, M. Q. Chang, J. C. Yang, Y. D. Guo, L. Ding, L. D. Yu, H. Huang, Y. Chen and J. L. Shi, *Adv. Funct. Mater.*, 2021, **31**, 2005093.

97 Y. Y. Fan, W. C. Zhou, X. Y. Qiu, H. D. Li, Y. H. Jiang, Z. H. Sun, D. X. Han, L. Niu and Z. Y. Tang, *Nat. Sustain.*, 2021, **4**, 509–515.

98 J. Di and W. Jiang, *Mater. Today Catal.*, 2023, **1**, 100001.

99 N. Tian, C. Hu, J. Wang, Y. Zhang, T. Ma and H. Huang, *Coordin. Chem. Rev.*, 2022, **463**, 214515.

100 K. Endo, M. Saruyama and T. Teranishi, *Nat. Commun.*, 2023, **14**, 4241.

101 B. Xiao, C. C. Shen, Z. G. Luo, D. Q. Li, X. Y. Kuang, D. K. Wang, B. Y. Zi, R. H. Yan, T. P. Lv, T. Zhou, J. Zhang and Q. J. Liu, *Chem. Eng. J.*, 2023, **468**, 143650.

102 Y. Shen, C. J. Ren, L. R. Zheng, X. Y. Xu, R. Long, W. Q. Zhang, Y. Yang, Y. C. Zhang, Y. F. Yao, H. Q. Chi,

J. L. Wang, Q. Shen, Y. J. Xiong, Z. G. Zou and Y. Zhou, *Nat. Commun.*, 2023, **14**, 1117.

103 M. Shahrezaei, S. M. H. Hejazi, H. Kmentova, V. Sedajova, R. Zboril, A. Naldoni and S. Kment, *ACS Appl. Mater. Interfaces*, 2023, **15**, 37976–37985.

104 G. M. Ren, J. Y. Zhao, Z. H. Zhao, Z. Z. Li, L. Wang, Z. S. Zhang, C. H. Li and X. C. Meng, *Angew. Chem., Int. Ed.*, 2023, **63**, e202314408.

105 W. J. Huang, H. B. Ming, X. Q. Bian, C. Yang, Y. D. Hou, K. N. Ding and J. S. Zhang, *Chem. Eng. J.*, 2023, **473**, 145230.

106 J. Di, C. Chen, Y. Wu, Y. Zhao, C. Zhu, Y. Zhang, C. Wang, H. Chen, J. Xiong, M. Xu, J. Xia, J. Zhou, Y. Weng, L. Song, S. Li, W. Jiang and Z. Liu, *Adv. Mater.*, 2022, **34**, 2204959.

107 H. Ou, Y. Qian, L. Yuan, H. Li, L. Zhang, S. Chen, M. Zhou, G. Yang, D. Wang and Y. Wang, *Adv. Mater.*, 2023, **35**, 2305077.

108 Z. Li, Z. Zhao, S. Chen, W. Wu, J. Ying Jin, U. Mao, Y. Lin and Y. Jiang, *Adv. Healthcare Mater.*, 2023, **13**, 2302480.

109 B. Sun, X. Wang, Z. Ye, J. Zhang, X. Chen, N. Zhou, M. Zhang, C. Yao, F. Wu and J. Shen, *Adv. Sci.*, 2023, **10**, 2207507.

110 S. Yougbare, H. L. Chou, C. H. Yang, D. I. Krisnawati, A. Jazidie, M. Nuh and T. R. Kuo, *J. Hazard. Mater.*, 2021, **407**, 124617.

111 S. Chen, D. Huang, M. Cheng, L. Lei, Y. Chen, C. Zhou, R. Deng and B. Li, *J. Mater. Chem. A*, 2021, **9**, 196–233.

112 J. Xiong, J. Di and H. Li, *J. Mater. Chem. A*, 2021, **9**, 2662–2677.

113 Y. Zhou, Z. Zhao, F. Wang, K. Cao, D. E. Doronkin, F. Dong and J.-D. Grunwaldt, *J. Hazard. Mater.*, 2016, **307**, 163–172.

114 S. Weng, Z. Fang, Z. Wang, Z. Zheng, W. Feng and P. Liu, *ACS Appl. Mater. Interfaces*, 2014, **6**, 18423–18428.

115 J. Sun, J. Wen, G. Wu, Z. Zhang, X. Chen, G. Wang and M. Liu, *Adv. Funct. Mater.*, 2020, **30**, 2004108.

116 L. Ye, X. Jin, X. Ji, C. Liu, Y. Su, H. Xie and C. Liu, *Chem. Eng. J.*, 2016, **291**, 39–46.

117 F. Chen, H. Huang, L. Ye, T. Zhang, Y. Zhang, X. Han and T. Ma, *Adv. Funct. Mater.*, 2018, **28**, 1804284.

118 Q. Zhang, L. Jiang, J. Wang, Y. Zhu, Y. Pu and W. Dai, *Appl. Catal., B*, 2020, **277**, 119122.

119 W. Yang and Y. Wang, *Appl. Catal., B*, 2021, **282**, 119574.

120 X. Zhang, B. Xu, S. Wang, X. Li, C. Wang, Y. Xu, R. Zhou, Y. Yu, H. Zheng, P. Yu and Y. Sun, *Appl. Catal., B*, 2022, **306**, 121119.

121 C. X. Zhu, Y. J. Wang, L. Y. Qiu, W. W. Yang, Y. S. Yu, J. M. Li and Y. Q. Liu, *J. Alloys Compd.*, 2023, **944**, 169124.

122 F. Xu, B. Chai, Y. Y. Liu, Y. L. Liu, G. Z. Fan and G. S. Song, *Colloids Surf., A*, 2022, **652**, 120950.

123 M. Tang, J. Wan, Y. Wang, G. Ye, Z. Yan, Y. Ma and J. Sun, *Water Res.*, 2024, **249**, 120950.

124 Y. Ji, Z. L. Song, Y. Xu and Y. L. Zhang, *J. Alloys Compd.*, 2022, **925**, 166655.

125 C. Y. Du, Y. Zhang, Z. Zhang, L. Zhou, G. L. Yu, X. F. Wen, T. Y. Chi, G. L. Wang, Y. H. Su, F. F. Deng, Y. C. Lv and H. Zhu, *Chem. Eng. J.*, 2022, **431**, 133932.

126 R. Chavan, N. Bhat, S. Parit, K. Narasimharao, R. S. Devan, R. B. Patil, V. C. Karade, N. V. Pawar, J. H. Kim, J. P. Jadhav and A. D. Chougale, *Mater. Chem. Phys.*, 2023, **293**, 126964.

127 S. Lee, B. Bayarkhuu, Y. Han, H. W. Kim, S. Jeong, C. Boo and J. Byun, *J. Membr. Sci.*, 2022, **660**, 120832.

128 J. R. Lin, P. F. Zhu, M. Liu, M. Duan, H. Lu and Z. X. Huang, *J. Alloys Compd.*, 2023, **960**, 170761.

129 A. Chachvalvutikul, T. Luangwanta, B. Inceesungvorn and S. Kaowphong, *J. Colloid Interface Sci.*, 2023, **641**, 595–609.

130 G. D. Fan, J. F. Zhou, F. Y. Ruan, Y. Li, H. Y. Tian, D. Fan, Q. Q. Chen and N. Li, *Sep. Purif. Technol.*, 2023, **309**, 123099.

131 W. Wei, Z. Wei, R. Li, Z. Li, R. Shi, S. Ouyang, Y. Qi, D. L. Philips and H. Yuan, *Nat. Commun.*, 2022, **13**, 3199.

132 Y. Shen, C. Ren, L. Zheng, X. Xu, R. Long, W. Zhang, Y. Yang, Y. Zhang, Y. Yao, H. Chi, J. Wang, Q. Shen, Y. Xiong, Z. Zou and Y. Zhou, *Nat. Commun.*, 2023, **14**, 1117.

133 Y. J. Zhang, Z. F. Xu, Q. Wang, W. C. Hao, X. Zhai, X. Fei, X. J. Huang and Y. P. Bi, *Appl. Catal., B*, 2021, **299**, 120679.

134 Y. Li, D. Hui, Y. Sun, Y. Wang, Z. Wu, C. Wang and J. Zhao, *Nat. Commun.*, 2021, **12**, 123.

135 P. Zhou, I. A. Navid, Y. Ma, Y. Xiao, P. Wang, Z. Ye, B. Zhou, K. Sun and Z. Mi, *Nature*, 2023, **613**, 66–70.

136 X. Yan, M. Xia, H. Liu, B. Zhang, C. Chang, L. Wang and G. Yang, *Nat. Commun.*, 2023, **14**, 1741.

137 X. Xin, Y. Zhang, R. Wang, Y. Wang, P. Guo and X. Li, *Nat. Commun.*, 2023, **14**, 1759.

138 X. Tao, H. Zhou, C. Zhang, N. Ta, R. Li and C. Li, *Adv. Mater.*, 2023, **35**, e2211182.

139 X. Y. Dong, Z. Y. Yin, L. Xu, J. H. Ma, H. M. Cao, Y. J. Li, Q. Wang, J. Han, J. B. Qiu, Z. W. Yang and Z. G. Song, *Ceram. Int.*, 2024, **50**, 4083–4091.

140 Z. R. Qian, L. Zhang, Y. F. Zhang and H. Cui, *Sep. Purif. Technol.*, 2023, **324**, 124581.

141 W. L. Dai, P. Wang, J. F. Long, Y. Xu, M. Zhang, L. X. Yang, J. P. Zou, X. B. Luo and S. L. Luo, *ACS Catal.*, 2023, **13**, 2513–2522.

142 L. Y. Zhao, W. L. Fang, X. C. Meng, L. Wang, H. C. Bai and C. H. Li, *J. Alloys Compd.*, 2022, **910**, 164883.

143 Z. Saddique, M. Imran, A. Javaid, F. Kanwal, S. Latif, J. C. S. D. Santos, T. H. Kim and G. Boczkaj, *Int. J. Hydrogen Energy*, 2024, **52**, 594–611.

144 S. A. Monny, Z. Wang, M. Konarova and L. Wang, *J. Energy Chem.*, 2021, **61**, 517–530.

145 J. Hu, C. Chen, Y. Zheng, G. Zhang, C. Guo and C. M. Li, *Small*, 2020, **16**, 2002988.

146 Z. Zhu, S. Wan, Y. Zhao, Y. Gu, Y. Wang, Y. Qin, Z. Zhang, X. Ge, Q. Zhong and Y. Bu, *Mater. Rep.: Energy*, 2021, **1**, 100019.

147 Y. Ji, M. She, X. Bai, E. Liu, W. Xue, Z. Zhang, K. Wan, P. Liu, S. Zhang and J. Li, *Adv. Funct. Mater.*, 2022, **32**, 2201721.

148 C. Tedesco and L. Malavasi, *Molecules*, 2023, **28**, 594–611.

149 S. Wu, J. Sun, Q. Li, Z. D. Hood, S. Yang, T. Su, R. Peng, Z. Wu, W. Sun, P. R. C. Kent, B. Jiang and M. F. Chisholm, *ACS Appl. Mater. Interfaces*, 2020, **12**, 20067–20074.

150 M. Hosseini, Z. Ahmadi, M. Khoobi, S. Dehghani and A. Kefayat, *ACS Sustainable Chem. Eng.*, 2020, **8**, 13085–13099.

151 L. Dong, P. Zhang, X. Liu, R. Deng, K. Du, J. Feng and H. Zhang, *ACS Appl. Mater. Interfaces*, 2019, **11**, 7774–7781.

152 S. M. Zhou, D. K. Ma, S. H. Zhang, W. Wang, W. Chen, S. M. Huang and K. Yu, *Nanoscale*, 2016, **8**, 1374–1382.

153 M. S. Kandanapitiye, M. Gao, J. Molter, C. A. Flask and S. D. Huang, *Inorg. Chem.*, 2014, **53**, 10189–10194.

154 C. Dai, R. Hu, C. Wang, Z. Liu, S. Zhang, L. Yu, Y. Chen and B. Zhang, *Nanoscale Horiz.*, 2020, **5**, 857–868.

155 Y. Xiong, F. Sun, P. Liu, Z. Yang, J. Cao, H. Liu, P. Liu, J. Hu, Z. Xu and S. Yang, *Chem. Eng. J.*, 2019, **378**, 122172.

156 L. Song, X. Dong, S. Zhu, C. Zhang, W. Yin, X. Zhang, X. Liu and Z. Gu, *Adv. Healthcare Mater.*, 2018, **7**, e1800830.

157 Y. Q. Zhang, C. Lin, Q. Lin, Y. B. Jin, Y. H. Wang, Z. Z. Zhang, H. X. Lin, J. L. Long and X. X. Wang, *Appl. Catal., B*, 2018, **235**, 238–245.

158 D. Ayodhya and G. Veerabhadram, *Mater. Today Chem.*, 2020, **17**, 100320.

159 P. Chen, H. Liu, W. Cui, S. C. Lee, L. A. Wang and F. Dong, *EcoMat*, 2020, **2**, e12047.

160 Y. Cheng, Y. Chang, Y. Feng, H. Jian, X. Wu, R. Zheng, K. Xu and H. Zhang, *Adv. Mater.*, 2019, **31**, e1806808.